

# REPORT DOCUMENTATION PAGE

Form Approved  
OMB No. 0704-0188

Public reporting burden for this collection of information is estimated to average 1 hour per response, including the time for reviewing instructions, searching existing data sources, gathering and maintaining the data needed, and completing and reviewing the collection of information. Send comments regarding this burden estimate or any other aspect of this collection of information, including suggestions for reducing this burden, to Washington Headquarters Services, Directorate for Information Operations and Reports, 1215 Jefferson Davis Highway, Suite 1204, Arlington, VA 22202-4302, and to the Office of Management and Budget, Paperwork Reduction Project (0704-0188), Washington, DC 20503.

1. AGENCY USE ONLY (Leave blank)	2. REPORT DATE	3. REPORT TYPE AND DATES COVERED	
	1/13/97	Final Technical Report; 2/01/96-10/31/96	
4. TITLE AND SUBTITLE  Light Scattering Induced by Turbulent Flow: A Numerical Study			5. FUNDING NUMBERS  N00014-96-1-0420
6. AUTHOR(S) J.A. Domaradzki			
7. PERFORMING ORGANIZATION NAME(S) AND ADDRESS(ES)  University of Southern California Department of Aerospace Engineering 854 W. 36th Pl., RRB 101 Los Angeles, CA 90089-1191			8. PERFORMING ORGANIZATION REPORT NUMBER
9. SPONSORING/MONITORING AGENCY NAME(S) AND ADDRESS(ES)  Dr. Steven Ackleson Office of Naval Research 800 North Quincy Arlington, VA 22217-5660 Attn: Environmental Optics Program			10. SPONSORING/MONITORING AGENCY REPORT NUMBER
11. SUPPLEMENTARY NOTES			
12a. DISTRIBUTION/AVAILABILITY STATEMENT  Approved for public release; distribution unlimited		12b. DISTRIBUTION CODE	
13. ABSTRACT (Maximum 200 words)  The direct numerical simulations of the temperature field in water were used to investigate light scattering caused by turbulent temperature inhomogeneities and to compare it with scattering caused by typical seawater particulates in two extreme cases: coastal and open ocean conditions. The particle contribution was simulated using Mie theory aided by theoretical considerations to describe scattering at small angles. Distributions of particles observed in an open ocean and a coastal environment were used. For the open ocean case study, we have assessed typical oceanic turbulence levels for the near-surface. We find that scattering due to simulated turbulence may dominate scattering due to particulates for small angles up to 10°. In the coastal ocean case, simulated turbulence may dominate scattering up to 5°. We have found that the scattering angle variance for a light beam propagating over 0.25m pathlength in the oceanic water can be as large as 0.1°.			
DTIC QUALITY INSPECTED 4			
14. SUBJECT TERMS  light scattering, turbulence, particulates, coastal waters		15. NUMBER OF PAGES 63	
		16. PRICE CODE	
17. SECURITY CLASSIFICATION OF REPORT Unclassified	18. SECURITY CLASSIFICATION OF THIS PAGE Unclassified	19. SECURITY CLASSIFICATION OF ABSTRACT Unclassified	20. LIMITATION OF ABSTRACT UL



January 15, 1997

School of Engineering  
Aerospace Engineering

Dr. Steven Ackleson  
ONR 322OP  
Ballston Centre Tower One  
800 North Quincy Street  
Arlington, VA 22217-5660

Ref: N00014-96-1-0420  
USC 53-4514-5020

Dear Steve:

Enclosed are three copies of the Final Technical Report for the above-referenced grant entitled "Light Scattering Induced by Turbulent Flow: A Numerical Study". Please do not hesitate to contact me if you need further information.

Sincerely,

J.A. Domaradzki  
Principal Investigator

Encl: as noted

cc: Adm. Grants Officer  
Defense Technical  
NRL  
ONR OOCC1  
USC Contracts and Grants

# Chapter 1

## Introduction: source of turbulent flow inhomogeneities in the oceanic flows

### 1.1 Introduction

The passage of a coherent electromagnetic beam through a turbulent medium results in a change of light velocity which in turn causes distortion in intensity and phase of the beam. Light propagation through the Earth's atmosphere has been studied extensively and many models have been developed to describe atmospheric turbulence (see for example the review by Strohbehn [67]). To date similar studies of the propagation of light in turbulent water are very sparse [71]. Field measurements of small-angle scattering [55] show that the volume scattering function exhibits a sharp peak which is orders of magnitude greater than that obtained from either the laboratory measurements of Spinrad [63] or Mie type calculations for non-turbulent conditions [62]. This effect (*i.e.* peaking of volume scattering function at small angles) has been attributed to scattering by turbulence-induced inhomogeneities in the refractive index of sea water [77]. One of the main goals of this work is to verify this conjecture.

Currently, increased use of optical detectors in the marine environment (for example biological oceanography and in underwater imaging and communications) makes quantifying the role of turbulence an important task. Fortunately, only small-scale fluctuations in the refractive index due to the flow field are relevant for light propagation. These small-scale features are only weakly dependent on the large-scale flow and thus are similar for different flow types [3].

The interaction of light with fluid inhomogeneities associated with turbulence has long been utilized in laboratory observations of turbulence (*i.e.*, using the shadowgraph technique) [73]. This technique has also been used *in situ*, *e.g.* to visualize a double-diffusive instability [42].

It is extremely difficult to accurately measure nearforward light scattering due to the existence of the primary light beam; likewise any simplifying assumptions about the structure of turbulent flow fields can lead to unexpected errors [72]. Thus I have chosen to use numerical simulation to investigate light propagation through a turbulent medium.

## 1.2 Inhomogeneities in the refractive index

Inhomogeneities in the refractive index (IRI) are characteristic of turbulent flows. Under typical oceanic conditions, these inhomogeneities appear to be temperature dominated. In general, however, the real part of the refractive index of seawater varies with changes of temperature, salinity, and pressure (changes in the imaginary part of the refractive index of water are negligibly small compared with the real part [8]). The effect of pressure can be neglected for spatial scales on the order of a meter or smaller. The variance of the IRI (assuming that salinity and temperature fields are not correlated) can be expressed as the sum of the variance associated with temperature and salinity:  $\overline{(n^2)}^{1/2} = \overline{(n_T^2)}^{1/2} + \overline{(n_S^2)}^{1/2}$ , where  $\overline{()}$  denotes spatial averaging,  $n$  is the refractive index, and  $n_T$  and  $n_S$  are the contributions of temperature and salinity respectively.

In the ocean, background temperature and salinity induce quite different variance in the IRI. For example, analysis of data from the coastal region off Oregon (Figure 3.5) show that variance of the refractive index due to temperature is much larger than that due to salinity (J. Moum, pers. comm.). Thus, only temperature-induced IRI will be considered in this study, so hereafter  $n = n_T$ . The contribution of the IRI to scattering has been postulated to be largest for the smallest IRI structures [77]. Therefore, in this study I will concentrate on light scattering by IRI structures at the smallest scale of temperature field. Since the behavior of temperature embedded in the turbulent field can be numerically simulated and then exhaustively studied,

we start with direct numerical simulation (DNS) of the temperature field in the turbulent flow.

## Chapter 2

# Direct numerical simulations of passive scalars with $Pr > 1$ advected by turbulent flow

### 2.1 Introduction

The spectral behavior of kinetic energy spectra in homogeneous, isotropic turbulence is fairly well established through results from experiments, theoretical studies, and numerical simulations. These studies have been reviewed in several monographs [49, 43]. For flows at high Reynolds numbers the most important part of the spectrum is the  $k^{-5/3}$  inertial subrange, which according to the Kolmogorov 1941 theory terminates below the Kolmogorov or dissipation wavenumber

$$k_K = (\epsilon/\nu^3)^{1/4} = 1/\eta_K, \quad (2.1)$$

where  $\epsilon$  is the kinetic energy dissipation rate,  $\nu$  is the kinematic viscosity, and  $\eta_K$  is the Kolmogorov length scale. Experimental results indicate that the inertial range ends around  $k \approx (0.1 - 0.2)k_K$ . Many theoretical and numerical results [39, 37, 18, 12, 44] support the following form for the dissipation range for wavenumbers  $k > 0.2k_K$

$$E(k) \sim (k/k_K)^\alpha \exp(-ak/k_K). \quad (2.2)$$

The exponential is well established and has been confirmed by the experiments of Sreenivasan [65] but the algebraic prefactor is uncertain though several investigations suggest  $\alpha \approx -2$  in the range  $0.2 < k/k_K < 4$ . While the inertial subrange exists only for sufficiently high Reynolds number turbulence, generally inaccessible to numerical

simulations, the dissipation range form (2.2) appears to be universally valid for all Reynolds numbers and can be easily simulated numerically. The universality in particular implies that those features of turbulence that are determined by scales from the vicinity of  $k_K$  can be investigated through direct numerical simulations (DNS) irrespective of Reynolds number. This observation is used later in our work.

In many physical situations one encounters passive scalars advected by turbulent velocity fields like temperature and pollutants in air and water. Following Kolmogorov's local isotropy hypothesis Obukhov [54] and Corrsin [14] predicted that scalar variance spectra at high Reynolds numbers will also have a  $k^{-5/3}$  inertial subrange. The behavior of the variance spectra for wavenumbers beyond the Corrsin-Obukhov range depends on the Prandtl (or Schmidt) number  $Pr = \nu/\kappa$ , where  $\kappa$  is the scalar diffusivity. For  $Pr < 1$  Batchelor *et al.* [4] predict the following form for the spectrum of the variance of a scalar advected by the velocity scales from the inertial subrange

$$E_\theta(k) \sim \chi \kappa^{-3} \epsilon^{2/3} k^{-17/3}, \quad (2.3)$$

where  $\chi$  is the scalar variance dissipation rate; the formula is valid for wavenumbers  $k$  greater than the Obukhov-Corrsin wavenumber,  $k_{OC}$

$$k_{OC} = (\epsilon/\kappa^3)^{1/4} = Pr^{3/4} k_K. \quad (2.4)$$

This form of the spectrum has been confirmed by the numerical simulations of Chasnov *et. al.* [11].

In oceanographic applications temperature and salinity are important scalars, and both have  $Pr > 1$ . The case of  $Pr \gg 1$  was investigated theoretically by Batchelor [3] who derived the following form of the scalar spectrum in the viscous-convective range

$$E_\theta(k) = -\frac{\chi}{\gamma} k^{-1} \exp(\kappa k^2 / \gamma), \quad (2.5)$$

where  $\gamma$  is the average value of the least principal rate of strain (a negative quantity) acting on scales  $k > k_K$ . The derivation is based on a physical picture of the scalar

field at scales  $k \gg k_K$  being deformed by an essentially uniform gradient of the velocity at much larger scales  $k \approx k_K$ . For  $k$  less than the Batchelor wavenumber

$$k_B = (\epsilon/\nu\kappa^2)^{1/4} = Pr^{1/2}k_K = 1/\eta_B, \quad (2.6)$$

the exponential factor in (2.5) is approximately equal to unity and the algebraic prefactor  $k^{-1}$  dominates such that the so-called Batchelor spectrum becomes

$$E_\theta(k) = -\frac{\chi}{\gamma}k^{-1}. \quad (2.7)$$

The final form of the Batchelor spectrum is determined by specifying the strain rate  $\gamma$ . For flows at high Reynolds numbers it is assumed that a good estimate is given by the rate-of-strain of Kolmogorov eddies

$$\gamma = -\frac{1}{q}(\epsilon/\nu)^{1/2}, \quad (2.8)$$

where  $q$  is a universal constant. Using available experimental data Batchelor [3] estimated  $q \approx 2$ . Gibson [22] provides a range of values  $\sqrt{3} < q < 2\sqrt{3}$  deduced from the incompressibility and kinematics of fluid elements. Oceanic measurements provided values of  $q = 3.9 \pm 1.5$  [27] and  $q = 3.7 \pm 1.5$  [53].

Each of the previous spectral predictions for scalar spectra results from a separate set of physical assumptions making the predictions independent of each other. Gibson [21] and [22] proposed a unified theory of passive scalars advected by turbulence valid for all values of the Prandtl number. The theory is based on the physical mechanism of generation of maxima and minima of the scalar concentration by the local rates of strain. This mechanism is distinctly different from the mechanism invoked by Batchelor for  $Pr \gg 1$ . While for  $Pr > 1$  Gibson's prediction for the spectra of the scalar is the same as Batchelor's prediction (2.5), for  $Pr \ll 1$  the Gibson's theory implies the intermediate  $k^{-3}$  range for  $k_{OC} < k < k_B$  before  $k^{-17/3}$  range develops for  $k > k_B$ . The evidence in support of Gibson's theory is discussed by Clay [13], and Kerr [37]. In the context of our work Gibson's analysis has two appealing features. First, it suggests that the Batchelor  $k^{-1}$  range may appear even if the Prandtl number is not much greater than unity (i.e. the condition  $Pr > 1$  replaces Batchelor's  $Pr \gg 1$ ). Second, it implies a universal scaling independent of

the Prandtl number for scalar spectra in the scalar dissipation range. This so-called Batchelor scaling is obtained by normalizing wavenumbers by the Batchelor length scale  $\eta_B$  and spectra by  $\chi(\nu/\epsilon)^{1/2}\eta_B$ . Under this scaling expression (2.5) is given by a self-similar form

$$\frac{E_\theta(k\eta_B)}{\chi(\nu/\epsilon)^{1/2}\eta_B} = q(k\eta_B)^{-1} \exp(-q(k\eta_B)^2). \quad (2.9)$$

Kraichnan [40] considered the effects of fluctuations of the rates of strain in space and time in Batchelor's analysis and showed that while  $k^{-1}$  behavior survives, the Gaussian factor in (2.5) is not universal and is replaced by a simple exponential. He also obtained the same result using Lagrangian-History-Direct-Interaction (LDHI) closure theory. Kraichnan's equation for a scalar spectrum was solved in a closed form by Mjolsness [48] giving the following result

$$E_\theta(k) = 5\frac{\chi}{\Lambda}k^{-1}(1 + \xi)\exp(-\xi), \quad (2.10)$$

where  $\xi = (30\kappa/\Lambda)^{1/2}k$ , and the constant  $\Lambda$  can be in principle calculated from the theory. By comparing functional expressions (2.10) and (2.7) in the limit  $k \rightarrow 0$  I get  $\Lambda = (5/q)(\epsilon/\nu)^{1/2}$ . Using the Batchelor scaling formula (2.10) becomes

$$\frac{E_\theta(k\eta_B)}{\chi(\nu/\epsilon)^{1/2}\eta_B} = q(k\eta_B)^{-1}(1 + (6q)^{1/2}k\eta_B)\exp(-(6q)^{1/2}k\eta_B). \quad (2.11)$$

Similar expressions, containing  $k^{-1}$  range and the exponential form, are also predicted by other analytical theories of turbulence [52, 29, 58]. The analytical theories also make predictions about the universal constant  $q$  in (2.11). Kraichnan [40] estimates  $q < 0.9$  using LHDIA, Newman and Herring [52] give  $q = 1.68$  using Test Field Model and Qian [58] gives  $q = 2\sqrt{5}$ . Only the last value is consistent with the experimental evidence.

In summary the classical picture of the scalar spectrum in high Reynolds number flow and  $Pr \gg 1$  as uniformly presented in turbulence literature [70, 49, 43] is the inertial  $k^{-5/3}$  behavior for  $k < k_K$ , the Batchelor  $k^{-1}$  behavior for  $k_K < k < k_B$ , and the exponential decay for  $k > k_B$ .

Despite the wealth of theoretical results in favor of this picture the experimental evidence is ambiguous, ranging from supporting to rejecting in part or entirely the spectral forms, in particular the  $k^{-1}$  Batchelor range, arrived at by theoretical consideration. Gibson and Schwarz [24] observed the Batchelor spectrum for temperature and salinity in laboratory measurements in water and the approximate  $k^{-1}$  behavior for temperature spectrum is also suggested by oceanographic field measurements of Grant *et al.* [27] and Oakey [53]. However, later measurements of Gargett [20] contradicted the universality of the Batchelor spectrum and cast doubt on earlier experimental results. Gibson [23] attributes Gargett's negative results to her failure to account for large intermittence of oceanic turbulence. The oceanographic implications of the discrepancy are summarized in the review of Gregg [28].

More recently Miller and Dimotakis [47] reported results of laboratory measurements of scalar spectra for high Schmidt number ( $\simeq 1.9 \cdot 10^3$ ) in a turbulent jet which does not show any evidence of the  $k^{-1}$  spectral behavior. Note that according to the Batchelor theory the large value of Schmidt number ( $\gg 1$ ) in this experiment should allow for an easy detection of the  $k^{-1}$  range. The  $k^{-1}$  range is also absent in the high Schmidt number 2-D mixing experiments of Gollub *et. al.* [25].

In addition, when the Batchelor range is in fact observed the quality of the experimental data often does not allow a clear distinction between the spectral forms (2.11) and (2.9) in the far-dissipation range. Consequently experimental results usually are interpreted assuming the earlier derived Batchelor spectrum (2.9) and no comparison studies with the Kraichnan spectrum are available. The practical importance of these spectral expressions lies in the fact that all scalar fluctuations and scalar dissipation are effectively determined by scales from the  $k^{-1}$  Batchelor range. The dissipation rates in turn determine the mixing coefficients for scalars [17] which are critical to understand the small-scale physics of the oceans as well as the large scale circulation and global climate. The knowledge of spatial power spectra of temperature fluctuations at small scales is also needed to address problems of sound and light propagation in water [69]. Several scalar models have been examined for those problems [30] but again lack of experimental data at the largest wavenumbers introduces uncertainties in the analyses. In view of the practical importance of the Batchelor spectrum and the scatter in the predicted values of the universal constant  $q$  as well as experimental controversies concerning the existence of the the

$k^{-1}$  range itself, further work in this area is clearly needed. Carefully designed numerical simulations may complement experiments and theory in contributing to the resolution of these controversies.

While numerical simulations have been used extensively to investigate scalar spectra for  $Pr \leq 1$  [37, 61, 57] no similar numerical effort has been devoted to the case of  $Pr > 1$ . The numerically discouraging aspect of this case is that substantially higher resolution is needed to simulate the scalar field than the velocity field. Indeed, the theoretically suggested location of the Batchelor spectrum,  $k > k_K$ , implies that the simulations should extend far into the dissipation range to values of  $k \gg k_K$ . This effectively limits the turbulence simulations on current supercomputers to very low values of the Reynolds number. However, two observations suggest that it may be possible to obtain the Batchelor spectrum in a properly designed numerical experiment despite the inability of DNS to simulate high Reynolds number flows. First, as already argued by Batchelor [3] the form of the relation (2.5) should also hold for low Reynolds number flows, as long as  $Pr \gg 1$  and there exist large velocity scales providing uniform rates of strain. More generally, the existence of the Batchelor range for scalars with  $Pr \gg 1$  can be viewed as a consequence of the scalar diffusion in a strain field that is spatially fairly uniform and random. This is persuasively demonstrated by the simple physical model of Antonsen *et al.* [2] where the extensive  $k^{-1}$  range was obtained by numerically solving the passive scalar equation with the velocity field prescribed as a long monochromatic wave with a random phase. A similar approach has been employed by Holzer and Siggia [33] for two-dimensional flows and by Pumir [57] for three-dimensional flows. In both cases only a few low wavenumber velocity modes, i.e. large scales, actively advect the passive scalar which is allowed to develop scales much smaller than the forcing velocity field. Holzer and Siggia [33] observed the  $k^{-1}$  range for simulations performed with  $512^2$  modes and hyperdiffusion while Pumir [57] estimates that in three dimensions the resolution of  $1000^3$  modes would be needed to observe the  $k^{-1}$  range. Also Metais and Lesieur [46] attribute an ‘anomalous’  $k^{-1}$  passive scalar range in their large eddy simulations to stirring of temperature by the large energy-containing eddies. While in many of these cases the  $k^{-1}$  range is observed, the prevailing rate of strain  $\gamma$  in (2.7) is generally different from the estimate (2.8), expected to hold only for high Reynolds number turbulence. Second, as noted above, there is evidence that the

energy dissipation range (2.2) is independent of (or only weakly dependent on) the Reynolds number. Therefore, the spectral dynamics of scales from the vicinity of the Kolmogorov wavenumber  $k_K$ , where the dissipation range is located, should be the same for large and small Reynolds number flows. When Kolmogorov scaling is used the increase in the Reynolds number only extends the energy spectrum to smaller wavenumbers without affecting scales from the vicinity of the Kolmogorov scale. Since Batchelor theory assumes that the scalar variance dynamics is driven by the Kolmogorov velocity scales, the universality of the energy dissipation spectra implies that the velocity field for a low Reynolds number turbulent flow should have the same effect on the scalar in the Batchelor range as a high Reynolds number flow. This observation suggests that it is plausible to expect not only the same  $k^{-1}$  spectral behavior, but also the same scaling, in particular for  $\gamma$ , to hold for all Reynolds numbers. Note, however, that previous numerical simulations performed for this problem [33, 57, 2] purposely did not attempt to simulate the dissipation range of the velocity field and thus were unable to address this issue.

In view of these arguments I believe that it is worthwhile to explore the dynamics of passive scalars for  $Pr > 1$  in low Reynolds number turbulent flows by numerically solving the full Navier-Stokes equation for velocity and a passive scalar.

## 2.2 Basic Equations and Numerical Methods

The flow dynamics are described by the incompressible Navier-Stokes equations for velocity  $\mathbf{u}(\mathbf{x}, t)$  and the transport equation for the passive scalar  $\theta(\mathbf{x}, t)$

$$\frac{\partial \mathbf{u}}{\partial t} + (\mathbf{u} \cdot \nabla) \mathbf{u} = -\frac{1}{\rho} \nabla p + \nu \nabla^2 \mathbf{u} + \mathbf{F}_u, \quad (2.12)$$

$$\nabla \cdot \mathbf{u} = 0, \quad (2.13)$$

$$\frac{\partial \theta}{\partial t} + (\mathbf{u} \cdot \nabla) \theta = \kappa \nabla^2 \theta + F_\theta. \quad (2.14)$$

In the equations  $\rho$  is a constant density,  $p$  is the pressure, and  $\nu$  and  $\kappa$  are the kinematic viscosity and the molecular diffusivity, respectively. The terms  $\mathbf{F}_u$  and  $F_\theta$  signify forcing added to the equations in order to obtain statistically stationary turbulence.

The flow is assumed to be contained in a cube of side  $L = 2\pi$  and periodic boundary conditions in all three spatial directions are imposed on the independent variables. The domain is discretized in physical space using  $N$  uniformly spaced grid points in each direction resulting in a mesh size  $\Delta x = L/N$  and a total of  $N^3$  grid points. The equations of motion are transformed to spectral space using the discrete Fourier transform

$$\mathbf{u}(\mathbf{k}) = \frac{1}{N^3} \sum_{\mathbf{x}} u(\mathbf{x}) \exp(-i\mathbf{k} \cdot \mathbf{x}), \quad (2.15)$$

and the inverse transform is

$$u(\mathbf{x}) = \sum_{\mathbf{k}} u(\mathbf{k}) \exp(i\mathbf{k} \cdot \mathbf{x}), \quad (2.16)$$

where  $\mathbf{x}$  are the mesh points in physical space and  $\mathbf{k}$  are the discrete wavenumbers with components  $k_i = \pm n_i \Delta k$ ,  $n_i = 0, 1, 2, \dots, N/2$ ,  $i = 1, 2, 3$ , and  $\Delta k = 2\pi/L = 1$ . The distinction between physical and spectral representation for a given quantity is made through its argument  $\mathbf{x}$  or  $\mathbf{k}$ , respectively.

The equations are solved using a pseudo-spectral numerical method of Rogallo [60] in the implementation of Yeung and Pope [76]. I have employed the forcing scheme of Sullivan *et al.* [68] in which the total energy of several low wavenumber modes is kept constant while evolution of individual modes through nonlinear interactions, subject to the global constraint, is allowed. Specifically, the sum of squared amplitudes of modes in a sphere of radius  $K_f = 2.5\Delta k$  is kept constant for both the velocity and the passive scalar. This is accomplished by multiplying all modes in the forced sphere by the same constant factor, usually not larger than 1.02, at the end of each time step. This restores the energy (or the scalar variance) in the sphere to the value at the beginning of the time step.

Physical quantities of interest for isotropic turbulence are described in terms of the scalar wavenumber  $k = |\mathbf{k}|$  by averaging over thin spherical shells defined for an arbitrary quantity  $f(\mathbf{k})$  as

$$\langle f(\mathbf{k}) \rangle = \frac{1}{N_k} \sum_{\mathbf{k}} f(\mathbf{k}), \quad (2.17)$$

where  $\langle \dots \rangle$  denotes the shell average and the summation extends over all  $N_k$  modes in the shell of thickness  $\Delta k$  centered at  $k = |\mathbf{k}|$ . The energy and the passive scalar spectra are defined as follows

$$E(k) = 4\pi k^2 \langle \frac{1}{2} u_n(\mathbf{k}) u_n^*(\mathbf{k}) \rangle, \quad (2.18)$$

$$E_\theta(k) = 4\pi k^2 \langle \theta(\mathbf{k}) \theta^*(\mathbf{k}) \rangle, \quad (2.19)$$

and the corresponding dissipation spectra are

$$D(k) = 2\nu k^2 E(k), \quad (2.20)$$

$$D_\theta(k) = 2\kappa k^2 E_\theta(k). \quad (2.21)$$

The integral of  $E(k)$  over  $k$  gives turbulent kinetic energy per unit mass  $3/2\bar{u^2} = 3/2u'^2$ , where the overbar denotes averaging in physical space and  $u'$  is the rms turbulent velocity, and the integral of  $E_\theta(k)$  gives the scalar variance  $\bar{\theta^2}$ . The integrated dissipation spectra give the dissipation rates of the kinetic energy,  $\epsilon$ , and of the scalar,  $\chi$ . The Taylor microscale is computed as  $\lambda = (15u'^2\nu/\epsilon)^{1/2}$  and the microscale Reynolds number is  $R_\lambda = u'\lambda/\nu$ . An important time scale for the evolution of turbulence is the large eddy turnover time  $T_e = L_p/u'$ , where  $L_p$  is the integral length scale

$$L_p = \frac{\pi}{2u'^2} \int_0^\infty k^{-1} E(k) dk. \quad (2.22)$$

$L_p$  is used to define the macroscale Reynolds number  $Re = u'L_p/\nu$  and the Peclet number  $Pe = u'L_p/\kappa = Pr Re$ .

Values of the velocity-derivative skewness  $S_u$  and the mixed-derivative skewness  $S_{u\theta}$  are often used in direct numerical simulations to assess how well turbulence is developed. The velocity derivative skewness  $S_u$  is given by the formula

$$S_u = \frac{\langle \left( \frac{\partial u_1}{\partial x_1} \right)^3 \rangle}{\langle \left( \frac{\partial u_1}{\partial x_1} \right)^2 \rangle^{3/2}}. \quad (2.23)$$

For isotropic turbulence the vorticity production rate is proportional to the velocity-derivative skewness  $S_u$ . The mixed-derivative skewness  $S_{u\theta}$

$$S_{u\theta} = \frac{\langle \left( \frac{\partial u_1}{\partial x_1} \right) \left( \frac{\partial \theta}{\partial x_1} \right)^2 \rangle}{\langle \left( \frac{\partial u_1}{\partial x_1} \right)^2 \rangle^{1/2} \langle \left( \frac{\partial \theta}{\partial x_1} \right)^2 \rangle}, \quad (2.24)$$

is related to the nonlinear transfer of scalar variance to small scales and takes a value zero when there is no net cascade to higher wavenumbers. For statistically steady isotropic turbulence  $S_u$  and  $S_{u\theta}$  may be expressed entirely in terms of energy and passive scalar spectra [36]

$$S_u = 2.35\nu \frac{\int k^4 E(k) dk}{(\epsilon/15\nu)^{\frac{3}{2}}} \quad (2.25)$$

$$S_{u\theta} = \frac{2}{15} \kappa \frac{\int k^4 E_\theta(k) dk}{(\epsilon/15\nu)^{\frac{1}{2}} (\chi/6\kappa)}. \quad (2.26)$$

## 2.3 Results

Calculations were carried out on the Cray C90 with resolution of up to  $240^3$  modes. In addition to the turbulent velocity field in each run we carried three passive scalars with values of the Prandtl number of 3, 5, and 7. The low wavenumber modes for both velocity and scalars were forced as described earlier. As an initial condition I used the prescribed energy spectrum proportional to the exponential  $E(k, 0) = C \exp(-ck)$ , where constants  $C$  and  $c$  were chosen for a given resolution to provide a prescribed value of the microscale Reynolds number. This form of the initial conditions is consistent with the experimental decay of the dissipation spectra at larger wavenumbers (2.2). Since low wavenumber modes  $0 < k \leq K_f = 2.5\Delta k$  are forced and excluded from the analysis, I did not attempt to match in the initial conditions the algebraic prefactor in (2.2). Equivalently, I could have initialized simulations with a constant energy spectrum for the forced modes  $k \leq K_f$  and vanishing spectrum for  $k > K_f$ , but such simulations would require longer time to reach a statistically stationary state. The initial scalar spectra were proportional to the energy spectrum. The simulations were started with the resolution of  $128^3$

modes and run for about one large eddy turnover time. Subsequently, the generated dataset was used as a restart for a run at higher resolution  $162^3$  which was allowed to evolve until a steady state for the scalar field was achieved (it takes longer for the scalar spectra to achieve equilibrium than for the energy spectra [57]). In this procedure at the restart time, the high wavenumber modes, outside the initial (smaller) spectral domain, are all zero. After the restart these modes evolve rapidly as they gain energy from the modes in the original smaller spectral domain by the nonlinear interactions. The change in the Reynolds number was accomplished by changing the viscosity. I found that this approach in increasing resolution minimizes the CPU time needed to generate a fully developed, statistically steady spectrum at the target resolution while still generating proper results. Turbulence parameters in all runs were chosen such that all energy and scalar spectra are well resolved in the final state. Due to computer time constraints the highest resolution case was run for about one large eddy turnover time after restarting from one of the  $162^3$  runs. Towards the end of this run the high wavenumber modes, initially zero at the restart time, still experience slight energy increase indicating imbalance between the nonlinear transfer and the dissipation in this part of the spectrum. However, the remaining parts of the spectrum are found in the statistical equilibrium and the velocity derivative skewness and the mixed-derivative skewness for this run attain generally accepted equilibrium values. These observations imply that simulated turbulence is sufficiently well developed for the purpose of our analysis which focuses on the  $k^{-1}$  behavior at low wavenumbers. Only results from the simulations performed with the higher resolutions of  $162^3$  and  $240^3$  modes are reported here. Parameters for these runs are gathered in Table 1 and Table 2.

Run	Resolution	$\nu$	$k_{max}$	$L_p$	$\lambda$	$\eta_K$	$u'$	$\epsilon$	$Re_\lambda$	$Re$	$-S_u$
<b>x162</b>	$162^3$	0.02	76	1.55	$\simeq 1.1$	0.111	0.44	0.052	$\simeq 25$	34	0.60
<b>aa162</b>	$162^3$	0.01	76	1.34	$\simeq 0.8$	0.0680	0.47	0.047	$\simeq 36$	62	0.46
<b>a240</b>	$240^3$	0.0033	113	1.09	$\simeq 0.4$	0.0259	0.56	0.080	$\simeq 77$	185	0.51

Table 2.1: Parameters of the simulations for the velocity field.

Run	$Pr$	$\eta_B$	$\chi$	$Pe$	$-S_{u\theta}$
<b>x162</b>	3	0.064	0.17	102	0.45
	5	0.050	0.16	170	0.42
	7	0.042	0.16	238	0.45
<b>aa162</b>	3	0.040	0.16	186	0.38
	5	0.030	0.19	310	0.40
	7	0.026	0.16	434	0.38
<b>a240</b>	3	0.015	0.26	555	0.41
	5	0.012	0.26	925	0.39
	7	0.0098	0.27	1295	0.36

Table 2.2: Parameters of the simulations for the scalar field.

Results for the spectra presented below are calculated using shell averages (2.17) with the first two forced shells removed and are suitably nondimensionalized bringing data from all runs to a self-similar form. The classical Kolmogorov scaling procedure for the energy spectra [37] uses  $\eta_K$  and  $(\epsilon\nu^5)^{1/4}$  for nondimensionalization of wavenumbers and spectra, respectively. For scalar spectra the Batchelor [3] scaling is usually employed where  $\eta_B$  and  $\chi(\nu/\epsilon)^{1/2}\eta_B$  are used to nondimensionalize wavenumber  $k$  and the spectra, respectively.

### 2.3.1 The velocity spectra

Fig. 2.1 presents log-log plot of three-dimensional energy spectra using the Kolmogorov scaling and multiplied by  $(k\eta_K)^{5/3}$ . For wavenumbers  $k\eta_K < 0.2$  the plotted functions appear flat which suggests a  $5/3$  slope for the energy spectra characteristic of the inertial range. This range of small wavenumbers is enlarged in Fig. 2.2 where

the vertical axis is plotted using a linear scale. The approximate inertial range is clearly present in run **a240** where the Kolmogorov constant  $C_K$  is between 1.2 and 1.6 for  $k\eta_K < 0.2$ . This value is consistent with the values observed experimentally but smaller than reported in numerical simulations where values around 2.0 are frequently found. No inertial range behavior is found for runs at lower Reynolds numbers. It is also clear that the Kolmogorov scaling succeeds in bringing spectra at different Reynolds numbers into a self-similar form. The values of the velocity derivative skewness  $S_u$  for all runs are given in Table 1 and are consistent with the generally accepted value of  $-0.5$  [36] for well developed turbulence. Fig. 2.3 presents the same quantity as in the previous figures but plotted on the log-linear scale which emphasizes the far dissipation range. In the far dissipation range the energy spectrum is believed to be a simple exponential, i.e  $E(k) \sim B \exp(-a\eta_K k)$ . Our data give value of  $B = 8.5$  and  $a = 5.4$  consistent with values of  $B = 8.4 \pm 0.6$  and  $a = 5.1 \pm 0.1$  of Kida and Murakami [38]. This fit is particularly good for the coefficient  $B$  due to large resolution of our runs and relatively poorer for the slope  $a$  because of the early termination of the **a240** run.

In Fig. 2.4 I plot the normalized kinetic energy dissipation spectra. In all cases the dissipation is concentrated at  $k\eta_K$  around  $(1 - 2) \times 10^{-1}$ . For the highest resolution case I observe the well defined dissipation peak but for the two cases at the lower resolution the maximum of the dissipation spectrum occurs at the smallest unforced wavenumbers. A complete overlap between the energy containing and the dissipation range is consistent with the lack of the inertial subrange in the latter cases.

### 2.3.2 The scalar variance spectra

In the previous subsection I showed that the energy spectra are self-similar and are consistent with other numerical and experimental results. This suggests that the numerically simulated velocity fields can be used to reliably advect passive scalars in order to study their dynamics. This suggestion is supported by the observed values of the mixed-derivative skewness  $S_{u\theta}$  in the simulations. One of the secondary predictions of Gibson's theory [22] is that the mixed derivative skewness is a constant independent of the Reynolds and Prandtl numbers. Numerical simulations of Kerr

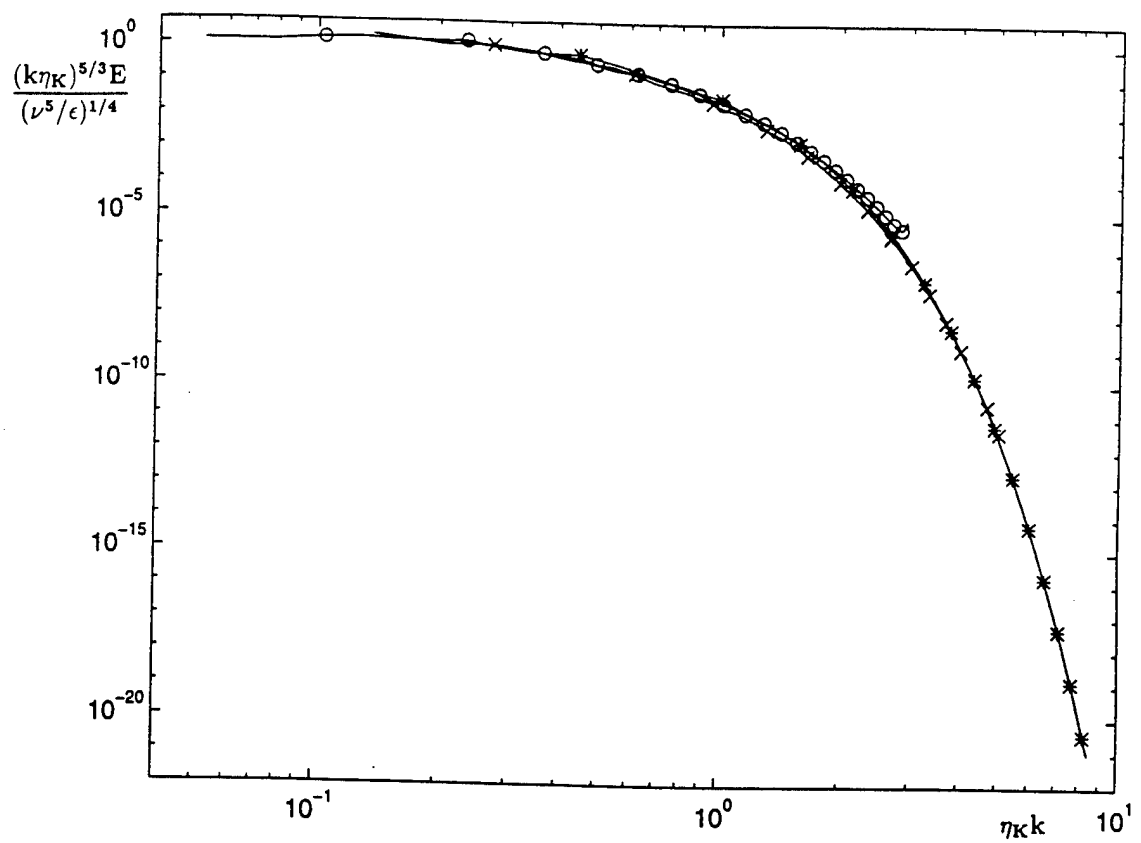


Figure 2.1: Normalized energy spectra  $E(k\eta_K)(k\eta_K)^{5/3}/(\epsilon\nu^5)^{1/4}$  for all runs (x-run aa162, o-run a240, \*-run x162).

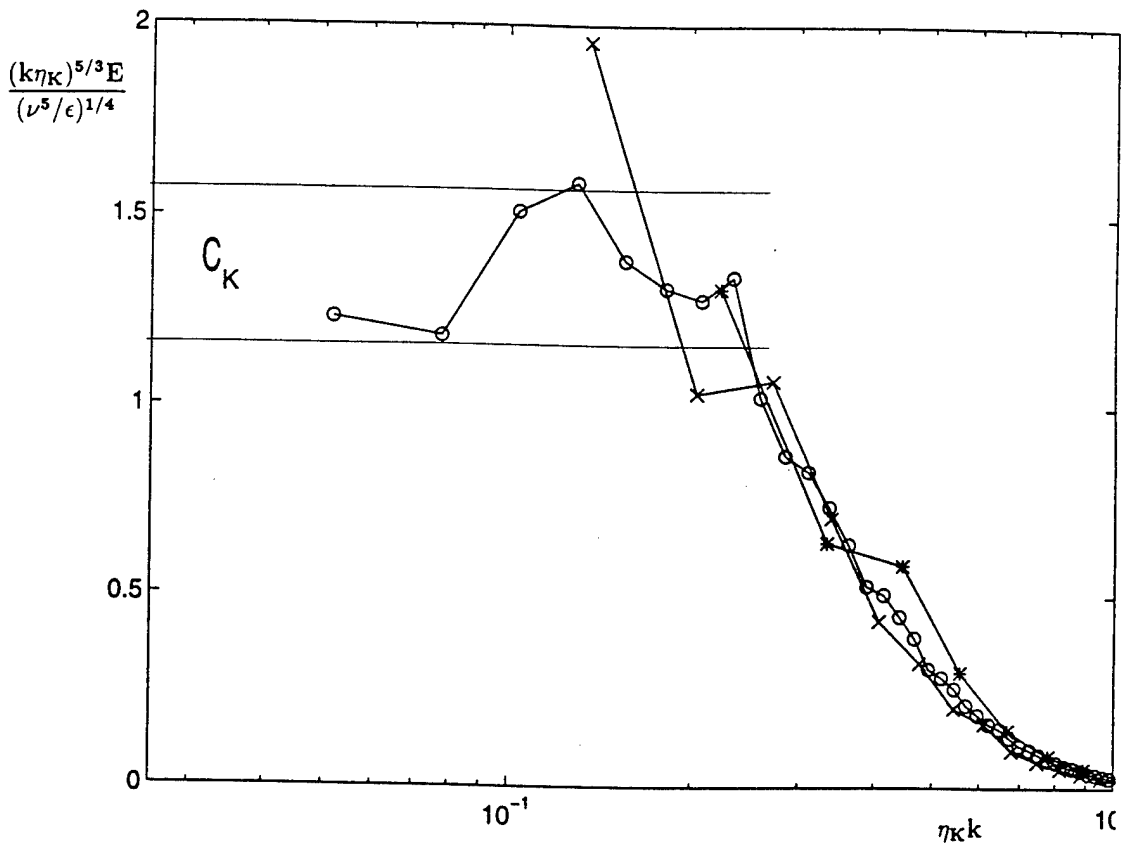


Figure 2.2: Normalized energy spectra  $E(k\eta_K)(k\eta_K)^{5/3}/(\epsilon\nu^5)^{1/4}$  in the range of low wavenumbers. The horizontal lines in the plot mark the range of values of the Kolmogorov constant (x-run aa162, o-run a240, \*-run x162).

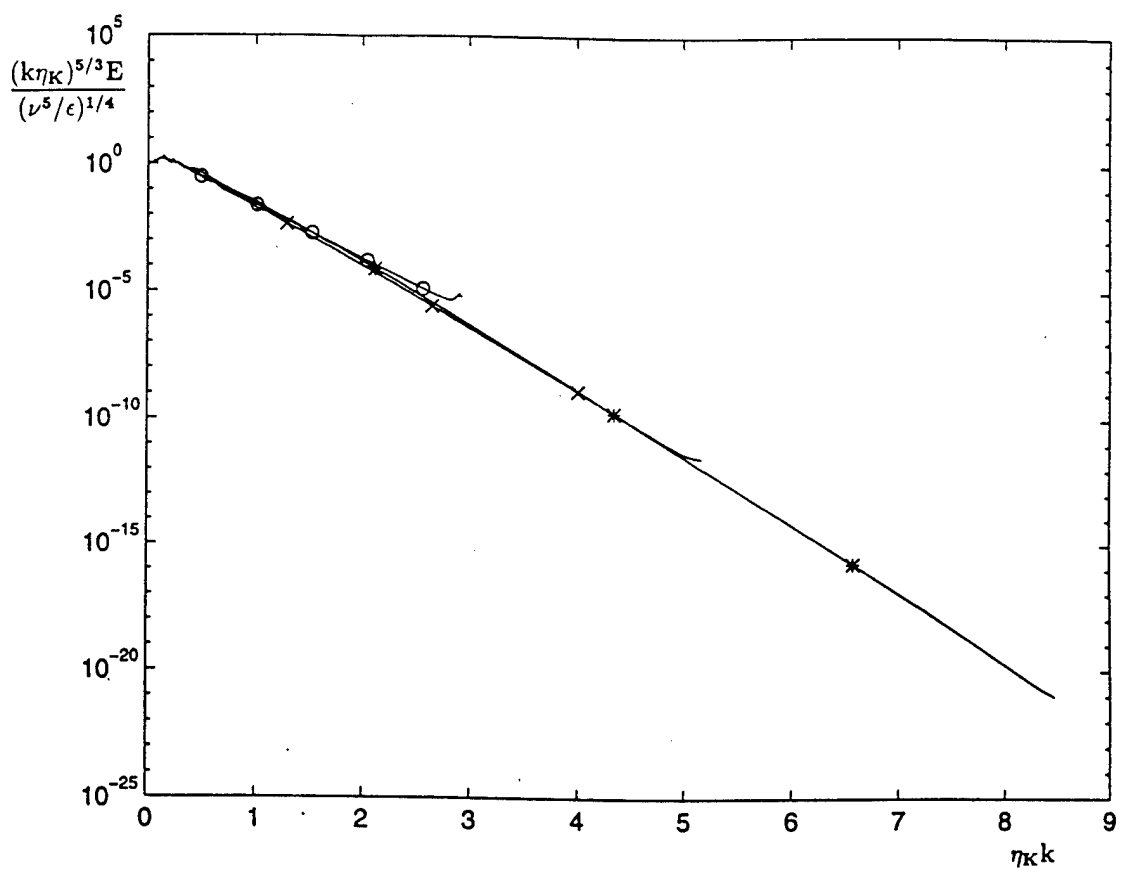


Figure 2.3: Normalized energy spectra  $E(k\eta_K)(k\eta_K)^{5/3}/(\epsilon\nu^5)^{1/4}$  plotted using log-linear scale to emphasize the exponential form (x-run **aa162**, o-run **a240**, \*-run **x162**).

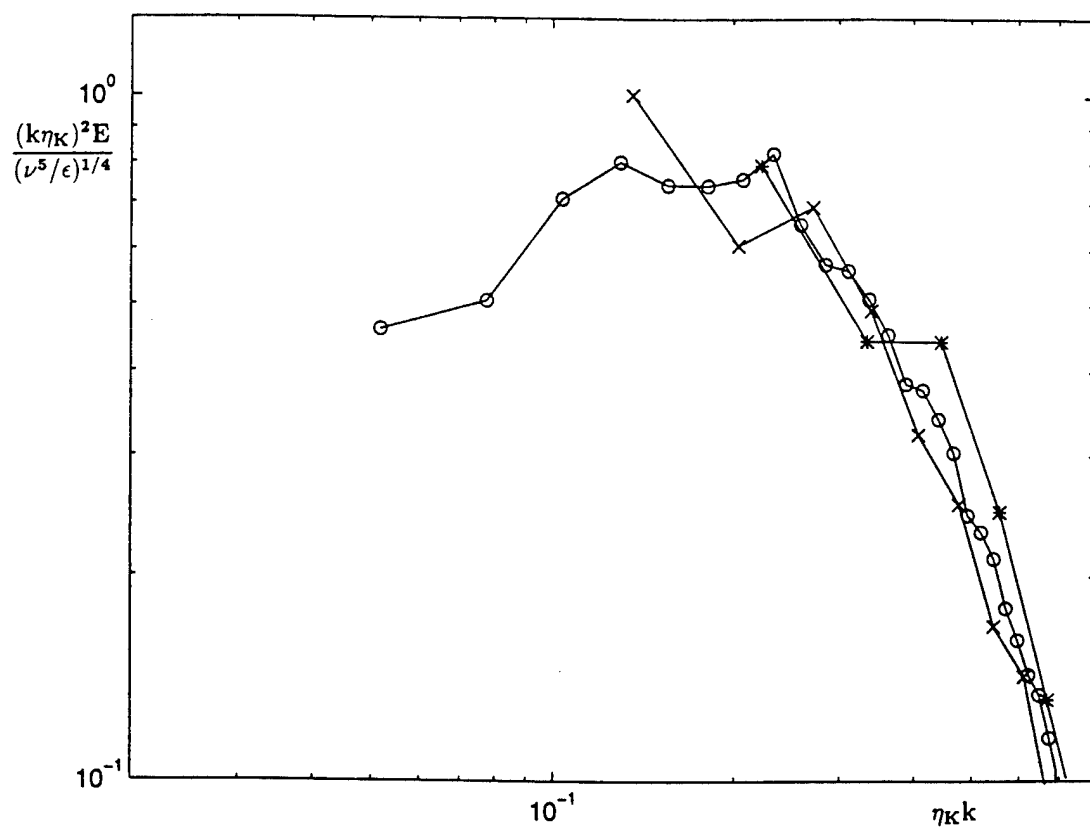


Figure 2.4: The normalized energy dissipation spectra  $E(k\eta_K)(k\eta_K)^2/(\epsilon\nu^5)^{1/4}$  in the range of low wavenumbers (x-run aa162, o-run a240, \*-run x162) .

[36, 37] agree with this prediction giving  $S_{u\theta} \simeq -0.5$ . The mixed derivative skewness is found to be around -0.4 in the experiments of Clay [13]. In our simulations  $S_{u\theta}$  is close to -0.4 for all analyzed runs (see Table 2). This also implies that the interactions between the velocity and scalar are well developed in the final states analyzed in this paper.

The controversial evidence for the existence of the Batchelor spectrum comes mostly from few laboratory and oceanographic measurements and numerical solutions of simplified model problems [10, 53, 24, 33, 57, 2]. To our knowledge there are no existing numerical simulations of full Navier-Stokes equations for passive scalar fields with  $Pr > 1$  which exhibit the Batchelor range behavior.

In Fig. 2.5 I plot the scalar spectra multiplied by  $k\eta_B$  using the Batchelor scaling for all three runs and all three Prandtl numbers  $Pr = 3, 5, 7$ . All curves collapse tightly to one universal form which shows that the Batchelor scaling is indeed universal for  $Pr > 1$  in the dissipation and the far dissipation range.

Because of the multiplication by  $k\eta_B$  the flat part of the curves in the range of small wavenumbers  $0.02 < k\eta_B < 0.2$  corresponds to the Batchelor range  $k^{-1}$  behavior which is observed in our simulations even for scalar with the Prandtl number as low as 3.

In Fig. 2.6 I plot the normalized dissipation spectra  $E_\theta(k\eta_B)(k\eta_B)^2/(\chi(\nu/\epsilon)^{1/2}\eta_B)$  for all cases. The Batchelor scaling clearly collapses the dissipation spectra for all Reynolds numbers and Prandtl numbers and the location of the dissipation peak around  $k\eta_B = 0.25$  is consistent with oceanic data of Oakey [53].

### 2.3.3 Parameters of the scalar spectra in the dissipation range

In the spectral forms proposed by Batchelor (2.9) and by Kraichnan (2.11) the constant  $q$  is unknown while all other parameters are either prescribed ( $\nu$  and  $\kappa$ ) or can be computed from the data ( $\epsilon$  and  $\chi$ ). Values of the universal constant  $q$  are obtained from the least square fit of formulas (2.9) and (2.11) to the numerical data for the run **a240** giving  $q_B = 3.9 \pm 0.25$  and  $q_{Kr} = 5.26 \pm 0.25$ , respectively. In Fig. 2.7 I present the results of the fit compared with the numerical data. Kraichnan's spectral form describes our data extremely well, with some exception in the exponential tail

corresponding to the scalar with  $Pr = 7$ . This can be attributed to the previously discussed fact that in this case the scalar field still evolves in the range of the largest wavenumbers. In the case of the Batchelor form the best fit curve Fig. (2.7) shows large systematic deviation from our numerical data. The systematic deviations of the Batchelor prediction from experimental data measured in situ has long been noted in oceanographic literature. Oakey [53] observed that in the  $k^{-1}$  portion of the spectrum the best fit to the Batchelor spectrum systematically underpredicts the experimental data. I observe similar behavior in our simulations (see Fig. 2.7), with the numerical data located above the Batchelor curve for wavenumbers before the dissipation peak. Our estimate of  $q_B = 3.9$  is in a good agreement with the value  $q = 3.7 \pm 1.5$  obtained by Oakey [53] from oceanic measurements.

Sometimes in oceanographic experiments the kinetic energy dissipation rate  $\epsilon$  is determined indirectly from the measured temperature variance spectra. This is accomplished by assuming that the temperature spectra are properly described by the Batchelor formula (2.9) with the assumed value of the universal constant  $q$ . The temperature variance dissipation rate  $\chi$  is computed directly from the measurements and  $\epsilon$  is treated as a parameter whose value is specified by requiring the best least squares fit of (2.9) to the measured data. This method based on the Batchelor spectral form is considered accurate within a factor of two. I have attempted to estimate the sensitivity/error in such a procedure associated with using either the Batchelor or the Kraichnan model. Several subsets of our data set (run **a240**) were selected such that the majority of the points either belonged to pre-peak, peak or the far dissipation range. In all sets the dissipation peak was resolved. Using earlier established optimum values of the constant  $q$ ,  $q_{Kr}$ , and  $q_B$ , this procedure yielded the relative error in estimated values of  $\eta_B$  up to 6% when using the Batchelor form and an order of magnitude less in the Kraichnan form case. Since  $\epsilon \propto \eta_B^4$ , fitting the Batchelor form to experimental data can account for at least 25% of the error in  $\epsilon$  estimates. In the presence of systematic measurement noise the error is expected to be larger. As argued by Gibson [23] the errors in estimating the dissipation rates from local measurements may be significantly larger if intermittence of turbulence is not properly taken into account. Because of the much smaller error implied by the Kraichnan formula its use should be attempted in estimating the kinetic

energy dissipation rates from the temperature variance measurements in oceanic environment.

### 2.3.4 One dimensional scalar spectra

The quantity usually measured in experiments is the one dimensional scalar spectrum  $E_{1\theta}$  which is related to its three dimensional counterpart  $E_\theta$  by the formula

$$E_\theta(k) = -k \frac{\partial E_{1\theta}(k)}{\partial k}, \quad (2.27)$$

and normalized as

$$\overline{\theta^2} = \int_0^\infty E_{1\theta}(k') dk' = \int_0^\infty E_\theta(k) dk, \quad (2.28)$$

We can obtain the one dimensional scalar spectrum derived both from the Batchelor and from the Kraichnan 3-D spectral form (2.9) and (2.11), respectively

$$\frac{E_{1\theta}(k)}{[\chi(\nu/\epsilon)^{1/2} \eta_B]} = q(k\eta_B)^{-1} \exp(-q(\eta_B k)^2) + \pi^{1/2} q^{3/2} (\text{erf}(q^{1/2}(\eta_B k)) - 1). \quad (2.29)$$

$$\frac{E_{1\theta}(k)}{[\chi(\nu/\epsilon)^{1/2} \eta_B]} = q(k\eta_B)^{-1} \exp(-(6q)^{1/2} \eta_B k). \quad (2.30)$$

In Fig. 2.8 I compare our calculated one dimensional scalar spectra with the above formulas. The Batchelor  $k^{-1}$  range corresponds to the flat part of the curves. Here as for the previous three-dimensional spectra, Batchelor's prediction agrees fairly well with the simulated data for small  $k$  but it diverges for larger wavenumbers ( $k\eta_B > 1$ ), while Kraichnan's model describes the spectrum very well in the entire range of simulated wavenumbers.

### 2.3.5 Location and universality of the $k^{-1}$ range

The remarkable fact is that Batchelor scaling, originally associated with the properties of high Reynolds number turbulence, works so well in our low Reynolds number simulations. Batchelor scaling uses the rate of strain of the Kolmogorov eddies  $(\epsilon/\nu)^{1/2}$  but one may argue that in our forced simulations the rate-of-strain of the

energy containing eddies  $u'/L_p$  is more appropriate. However, scaling based on  $u'/L_p$  did not bring the data to a self-similar form. The success of the Batchelor scaling supports the arguments put forward in the Introduction where I propose that the Batchelor range spectrum may be independent of Reynolds number because of the universality of the dissipation range spectrum. It also indirectly supports Gibson's [22] theory which predicts that the Batchelor scaling should apply to the scalar far dissipation range for arbitrary values of  $Pr$ , not necessarily for  $Pr \gg 1$  as first proposed by Batchelor [3]. The location of the simulated  $k^{-1}$  range for  $k\eta_B \leq 0.2$ , equivalent to roughly  $k\eta_K \leq 1$ , appears to be at variance with the Batchelor theory which predicts the  $k^{-1}$  range for wavenumbers  $k\eta_K \gg 1$ . However, the inconsistency is removed if one notes that the velocity scales responsible for the Batchelor range behavior should be those that provide the largest rates-of-strain. Since the spectral estimate of the rate-of-strain is  $(E(k)k^2)^{1/2}$ , generally the dominant scales are located in the vicinity of the maximum dissipation wavenumber  $k\eta_K \approx 0.2$  rather than around the Kolmogorov wavenumber  $k\eta_K \approx 1$ . Moreover, the extent and the location of the Batchelor range is consistent with the following Obukhov type argument [15]. The scalar variance flux  $F(k)$  at wavenumber  $k$  is estimated as

$$F(k) = kE_\theta(k)/\tau(k), \quad (2.31)$$

where  $\tau(k)$  is the turnover time for scales  $k$ . In Batchelor theory the scalar flux and the turnover time are independent of  $k$ ,  $F(k) = \chi$  and  $\tau \simeq (\nu/\epsilon)^{1/2}$ , respectively, resulting in

$$E_\theta(k) \sim \chi(\nu/\epsilon)^{1/2}k^{-1}. \quad (2.32)$$

In general the scalar flux is expected to be approximately constant in the range of wavenumbers with negligible scalar variance dissipation. As one progresses towards larger wavenumbers the scalar variance flux is steadily decreased by the dissipation, with the largest effect around the scalar dissipation peak. According to Fig. 2.6 the dissipation peak is located somewhere between  $(0.2 - 0.3)k\eta_B$ . Therefore, the previous arguments suggest that the Batchelor range should be observed for  $k < 0.2k\eta_B$ , which is indeed the case. In general the experimental results are consistent with the onset of the Batchelor range at around  $k\eta_K \simeq 0.05$  for Prandtl numbers ranging from  $Pr \simeq 1$  to  $Pr = 100$  [30]. In our data the beginning of the  $k^{-1}$  range

can be observed in Fig. 2.9 where the scalar spectra multiplied by  $k$  are plotted after normalizing wavenumbers with the Kolmogorov length  $\eta_K$  rather than with the Batchelor length  $\eta_B$ . With this normalization I obtain a family of self-similar curves, one for each different value of the Prandtl number. The extent of the  $k^{-1}$  range increases with the increasing value of  $Pr$  but all curves converge to a common origin at  $k\eta_K \approx 0.05$ .

## 2.4 Conclusions

We have examined energy and passive scalar spectra obtained in high resolution direct numerical simulations at three different Reynolds numbers and for three Prandtl numbers  $Pr = 3, 5$ , and  $7$ .

At the highest Reynolds number  $R_\lambda = 77$  the energy spectrum has a short inertial range and the Kolmogorov constant is consistent with experimental data. The lower Reynolds number cases do not exhibit the inertial range behavior. The maximum in the dissipation spectrum is found between  $0.1$  and  $0.2k\eta_K$ . In all cases the spectra in the far dissipation range for  $k\eta_K > 0.2$ , i.e. beyond the dissipation peak, have an universal exponential form independent of Reynolds number and with parameters in good agreement with other numerical investigations. The universality implies that those features of turbulence that are determined by scales from the vicinity of the dissipation peak and beyond can be investigated through direct numerical simulations irrespective of the value of the Reynolds number. In particular, since the Batchelor spectrum for passive scalars with  $Pr > 1$  is assumed to be controlled by the velocity scales from the vicinity of  $k\eta_K \approx 1$ , this suggests that passive scalars with  $Pr > 1$  advected by such turbulent velocity fields should exhibit universal behavior consistent with the predictions of Batchelor [3] and Gibson [22].

This conclusion is confirmed by the simulated passive scalar spectra. In all cases I observe the appearance of the Batchelor  $k^{-1}$  range followed by the exponential decay in wavenumber  $k$  and the spectra are self-similar under the Batchelor scaling. However, we find the Batchelor range behavior for wavenumbers  $k\eta_K \leq 1$ , at variance with the Batchelor theory which predicts the  $k^{-1}$  range for wavenumbers  $k\eta_K \gg 1$ . Our results suggest that the velocity scales responsible for the Batchelor range

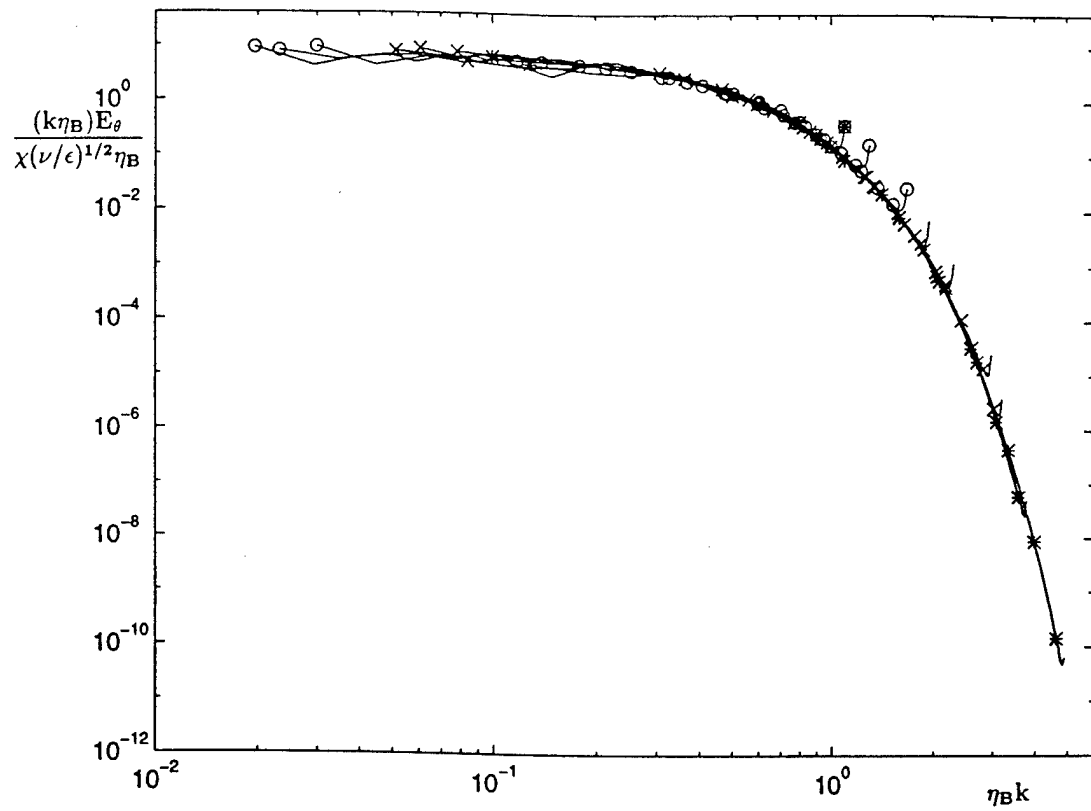


Figure 2.5: Normalized scalar spectra  $E_\theta(k\eta_B)(k\eta_B)/(\chi(\nu/\epsilon)^{1/2}\eta_B)$  for all runs and all Prandtl numbers (x-run **aa162**, o-run **a240**, \*-run **x162**).

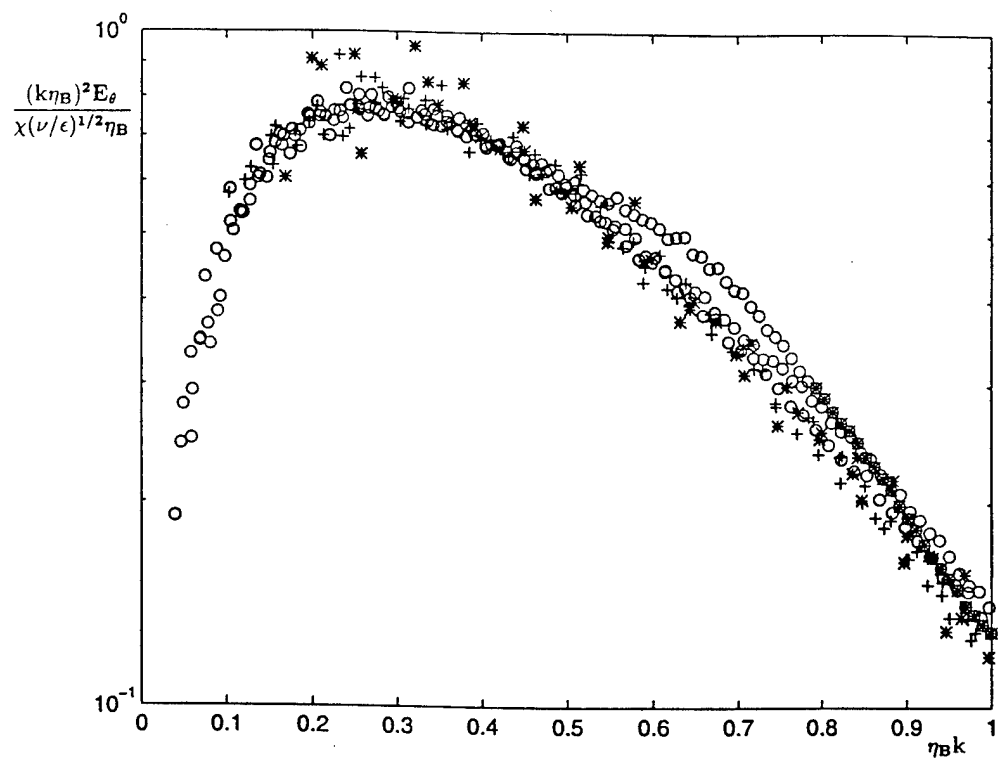


Figure 2.6: Normalized scalar dissipation spectra  $E_\theta(k\eta_B)(k\eta_B)^2/(\chi(\nu/\epsilon)^{1/2}\eta_B)$  for all runs and all Prandtl numbers (x-run **aa162**, o-run **a240**, \*-run **x162**).

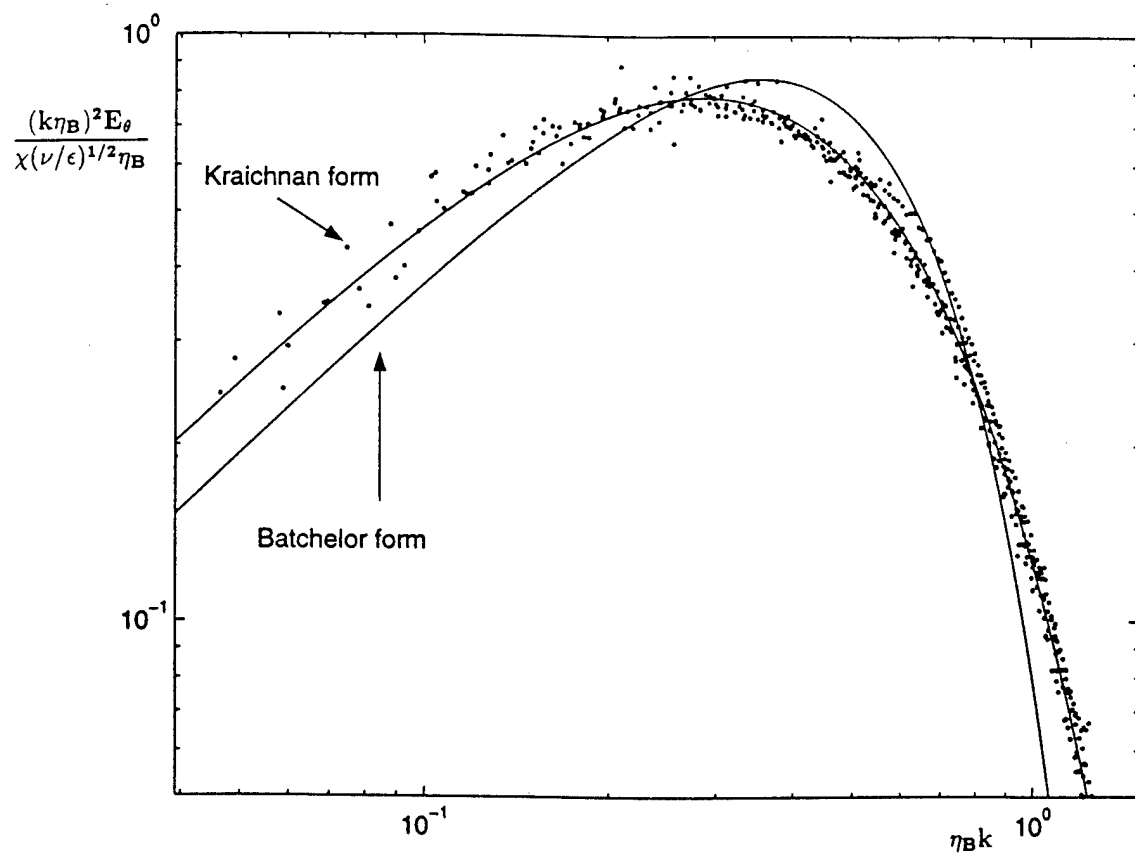


Figure 2.7: Normalized scalar dissipation spectra  $E_\theta(k\eta_B)(k\eta_B)^2/(\chi(\nu/\epsilon)^{1/2}\eta_B)$  for run **a240** and the best least squares fit provided the Kraichnan and Batchelor spectral forms.

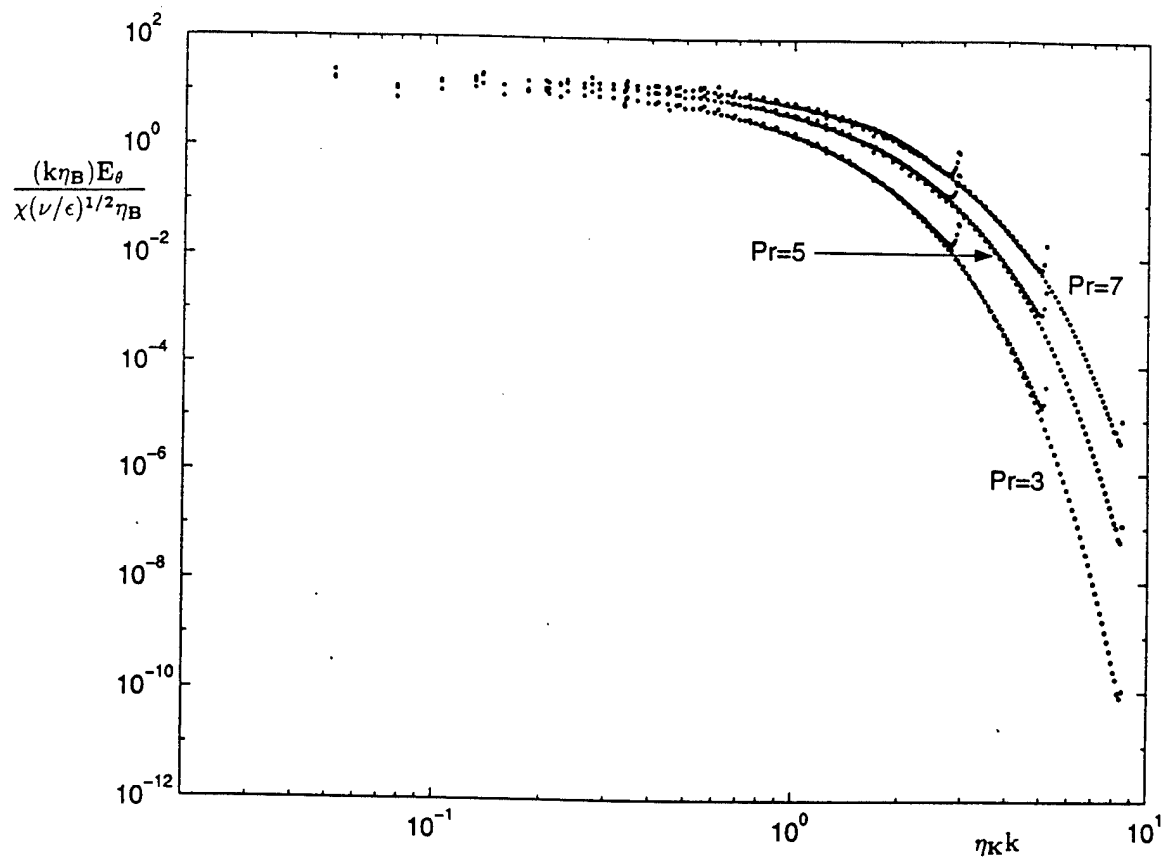


Figure 2.8: Normalized one dimensional scalar spectra  $E_\theta(k\eta_K)(k\eta_K)/(\chi(\nu/\epsilon)^{1/2}\eta_B)$  for all runs and all Prandtl numbers with wavenumbers nondimensionalized by the Kolmogorov scale. For comparison the Kraichnan (2.30) formula and the frequently used Batchelor expression (2.29) are plotted.

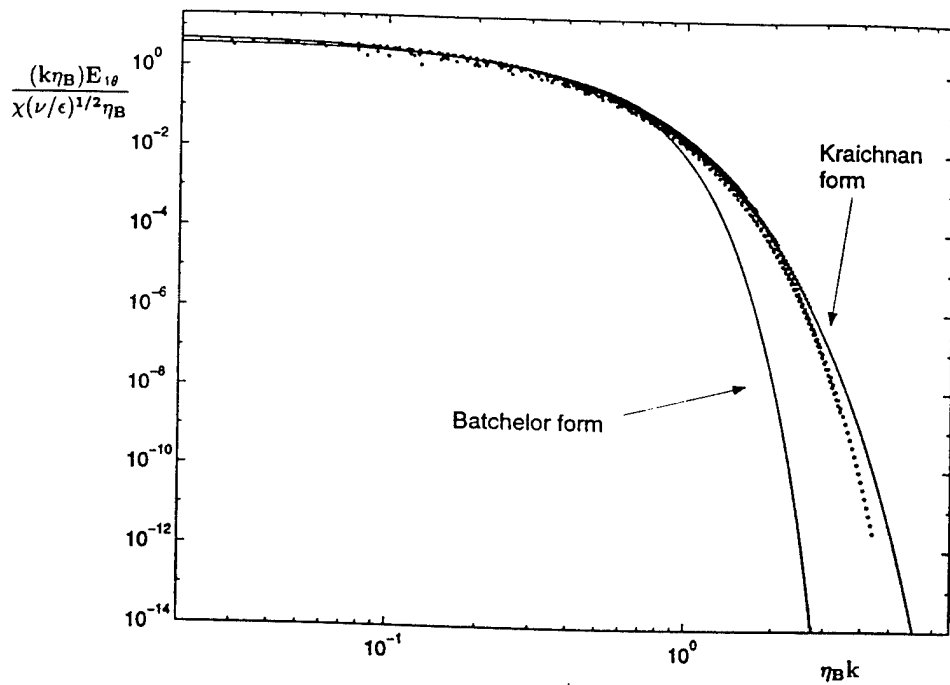


Figure 2.9: Normalized scalar spectra  $E_\theta(k\eta_K)(k\eta_K)/(\chi(\nu/\epsilon)^{1/2}\eta_B)$  for all runs and all Prandtl numbers with wavenumbers nondimensionalized by the Kolmogorov scale.

behavior reside in the vicinity of the maximum dissipation wavenumber  $k\eta_K \approx 0.2$  rather than around the Kolmogorov wavenumber  $k\eta_K \approx 1$ .

Comparisons with the Batchelor and Kraichnan functional forms of the scalar spectra show that data from our simulations follow closely the Kraichnan form while displaying systematic deviations from the Batchelor form. In the context of oceanographic procedures which estimate the kinetic energy dissipation rates  $\epsilon$  from the temperature measurements the implication is that the Kraichnan formula will provide more accurate estimates than the Batchelor formula.

Our numerical results contribute to the ongoing discussion concerning the form and universality of passive scalar spectra in turbulent flows for  $Pr > 1$ . It may be useful to summarize briefly several main differences between our assumptions and experimental conditions and those of other studies since they may responsible for the different conclusion reached. The values of the Prandtl number in the simulations (3, 5, and 7) are greater than unity but much less than those of some experiments [47]. Similarly, the values of Reynolds numbers in the simulations are much smaller than in many experiments but comparable to others [20]. The simulations are very well resolved in the range of small scales, much better than typical experiments or field measurements [53], allowing the clear distinction between the Gaussian and exponential fall-off at large  $k$ . Contrary to other numerical simulations [57] which restrict the velocity field responsible for advecting the scalar to only a few active modes, I use the full velocity field obtained from the Navier-Stokes equations. This may enable us to observe the  $k^{-1}$  range at smaller resolutions than suggested by other numerical models.

Finally, I believe that analyses of the velocity and scalar field using physical space representations are helpful in determining the precise physical mechanisms responsible for the Batchelor range behavior and I propose that such analysis be performed in the future.

## 2.5 Summary

Direct numerical simulations of passive scalars, with Prandtl numbers  $Pr = 3, 5$ , and 7, advected by turbulence at three low Reynolds numbers were performed. The

energy spectra are self-similar under the Kolmogorov scaling and exhibit behavior consistent with many other investigations: a short inertial range for the highest Reynolds number and the universal exponential form of the spectrum for all Reynolds numbers in the dissipation range. In all cases the passive scalar spectra collapse to a single self-similar curve under the Batchelor scaling and exhibit the  $k^{-1}$  range followed by an exponential fall-off. I attribute the applicability of the Batchelor scaling for our low Reynolds number flows to the universality of the energy dissipation spectra. The Batchelor range is observed for wavenumbers in general agreement with experimental observations but smaller than predicted by the classical estimates. The discrepancy is caused by the fact that the velocity scales responsible for the generation of the Batchelor range are in the vicinity of the wavenumber of the maximum energy dissipation, which is one order of magnitude less than the Kolmogorov wavenumber used in the classical theory. Two different functional forms of passive scalar spectra proposed by Batchelor and Kraichnan were fitted to the simulations results and I found that the Kraichnan model agrees very well with the data. The Batchelor formula displays large systematic deviations from the data and this fact may account for some portion of the observed experimental errors in oceanographic calculations which estimate the kinetic energy dissipation rates from temperature measurements.

## Chapter 3

### A comparison of the effects on near forward light scattering by turbulence and by particulates in the ocean

#### 3.1 Introduction

It has been proposed that the propagation of light in the ocean is affected by the presence of particulates and by inhomogeneities in seawater density caused by turbulence [55]. Hereafter, any process by which the direction of an individual photon is changed is referred to as scattering. In seawater the light beam direction can be changed in the near-forward regime either by interaction with water inhomogeneities or particulates. The role of particulates to determine the optical properties of oceanic waters is actively studied (*e.g.* Spinrad *et al.* [64]) while that of turbulence, though recognized (*e.g.* Honey [34]), is not commonly taken into account. Here I present evidence, obtained from numerical simulations and a preliminary laboratory experiment, that turbulence dominates scattering at small angles in oceanic waters.

Since air turbulence limits the resolving power of earth telescopes and other optical instruments the study of light propagation and scattering due to turbulence has played an important role in astronomic research for the last two decades. The recent progress of adaptive optics, which can now correct for atmospheric turbulence, has improved the resolution of earth telescopes to nearly the same resolution as their space (turbulence free) counterparts. A review of light propagation in the turbulent atmosphere is presented by Kravtsov [41].

The optical oceanography community has long acknowledged the effect of turbulence on light propagation in the ocean [75, 32, 34, 78]. Petzold [55] noted that the effect of turbulence is observed at small near forward angles of scattered light. However, the importance of turbulence on optical measurements remains controversial. This controversy is in large part due to the necessary complexity of the instrument technology and its underwater use. A numerical approach has been impeded because computers have not been able to accurately resolve details of turbulent flow with passive scalars such as temperature in the ocean, where smaller scales must be addressed than for the atmosphere. It is now possible to carry out numerical simulations, though they are very computer-intensive, and require hours of computation time on a supercomputer [5]. The results from these simulations were presented in the previous chapter.

By contrast, the role of particulates in the propagation of light in the ocean has received much attention. This is because, especially in the open ocean, phytoplankton are responsible for the variability of the optical properties [51]. Particulates not only scatter but also absorb light, thus removing light energy from the water column. When particulates scatter and redistribute light, forward scattering at small angles predominates over backscattering. In fact more than half of the scattered light is scattered at angles less than  $3^\circ$  [63]. The effect of particulates on scattering is a well researched subject for the case of spherical homogeneous particulates [7]. The study of scattering on particulates is guided by Mie theory [63, 62, 66].

The importance of near-forward scattering, summarized by Gordon [9], is in its effect on underwater imaging, the distribution of water-leaving radiance from the ocean surface, and on the measuring capabilities of underwater optical sensors. Small angle scattering can have a large effect on underwater optical imaging. This has become increasingly important as new time-gated imaging instruments are capable of imaging to five optical depths and more, representing typically a few tens of meters. As the range is increased, the smaller angles play a larger role. For remote sensing applications, even near an unscattered solar beam, the radiance distribution will depend on small-angle scattering. This will affect the water-leaving radiance. Likewise, optical instruments that measure particulate sizes rely on the details of near forward scattering. Additionally, underwater communication is degraded by

optical pulse stretching which depends directly on the value of near forward scattering. The transmission rate depends on the pulse width and is thus limited by small angle scattering processes.

I propose that turbulence-induced scattering is in fact responsible for most near forward scattering. The aim of this chapter is to compare the properties of the near-forward scattering on particulates and temperature inhomogeneities in seawater. I start first with scattering on particulates.

### 3.2 Scattering on particulates; open ocean and coastal example

In the course of this chapter I will use the volume scattering function (VSF)  $\beta(\alpha)$  as a variable to describe the scattering characteristics of the medium. The VSF describes the angular distribution of the scattered radiation as the scattered radiant intensity  $dI(\alpha)$  in a direction  $\alpha$  per unit scattering volume  $dV$  divided by the incident irradiance  $E_0$

$$\beta(\alpha) = \frac{dI(\alpha)}{E_0 dV}, \quad (3.1)$$

The associated scattering coefficient,  $b$ , describes how much light has been removed and scattered from the incident plane wave beam; it is defined as:

$$b = 2\pi \int_0^\pi \beta(\alpha) \sin(\alpha) d\alpha \quad (3.2)$$

It should be noted that the light beam is attenuated by both scattering and absorption processes and the corresponding attenuation coefficient,  $c$ , is given by  $c = a + b$ , (where  $a$  is the absorption coefficient). The attenuation coefficient parameterizes the exponential decay of the flux along the light beam as expressed by  $E(r) = E_0 \exp(-cr)$ , where  $r$  is a path length. The non-dimensional quantity  $cr$  is called the optical thickness. Even though all quantities,  $a$  and  $b$ , are in general wavelength-dependent, for the purpose of this work I will consider only one wavelength.

The VSF and  $b$  are considered inherent optical properties. Following Preisendorfer [56], these are properties whose magnitudes depend only on the substances

present in the water and independent of the geometrical structure of the various light fields that may pervade it. For turbulence this becomes less clear because of its statistical nature: a water column can only be characterized by a given turbulence level for short time periods. The VSF as defined above provides a good description of the medium with randomly organized structures like cells where we can assume that axial symmetry exists. However, it fails in the case of more organized media like crystals and it becomes difficult to interpret for turbulent media. I will use it nevertheless because it provides a useful framework to compare with available theories and experimental evidence of scattering in the ocean.

The superposition principle applies to all inherent coefficients and in the case of VSF it implies that if several substances are present in the medium, the global VSF results from the sum of the contributions from all constituents (as long as the single-scattering assumption is fulfilled). This allows me to calculate a total VSF in the case when the particulate ensemble is made up of particles of various size categories. In general, scattering by spherical particulates is exactly described by Mie theory. The parameters in this theory are refractive index, size, and scattering angle. Fortunately, scattering at small angles can be greatly simplified since it is nearly equivalent to diffraction by apertures of equal diameter [59] and it is insensitive to variation in the refractive index. This approximation is valid within a couple of percent up to angles of  $O(10^\circ)$ . The typical VSF for small angles due to diffraction for one particle is shown in Figure 3.1.

For our comparison I will use a particle size distribution that is characteristic of coastal waters [26] and the VSF standard for open ocean clean water [32]. The coastal particulate distribution was measured with a Coulter counter in the Bahama Banks. The measured distribution approximates a slope of -3 for the entire (cumulative) distribution. I then calculated the particle concentrations in individual size classes and multiplied the concentrations by the corresponding VSF for one particulate. The concentrations are plotted in Figure 3.2. The resultant VSF for angles up to  $30^\circ$  is shown in Figure 3.3. This VSF exhibits the typical properties as experimentally obtained by Spinrad [63], namely the flat plateau for angles of a few degrees and decreasing afterwards. The absolute value of the VSF for the coastal sample is higher by about a factor of 10, as would be expected for the larger concentrations and the presence of large cells and is consistent with the lower particulate

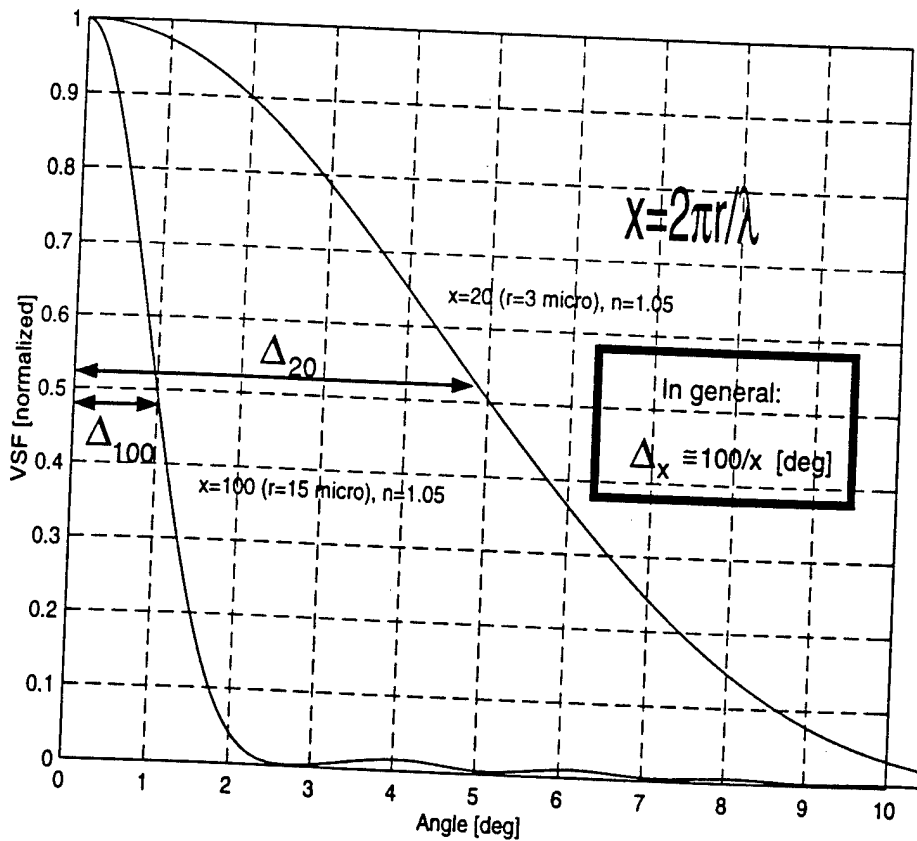


Figure 3.1: Normalized VSF, due to diffraction on a spherical particle, for a single sphere of size parameters  $x = 20$  and  $x = 100$ ; 3 and 15  $\mu m$  radius. The width of the near-forward VSF peak is given by  $\Delta = 100/x$  in  $^{\circ}$ .

concentrations used by Spinrad. The largest contribution to the value of the coastal VSF at small angles ( $\alpha \rightarrow 0$ ) are from the largest particulates of radius  $1000\mu m$ .

For the open ocean, I used the standard VSF form for clear open ocean waters proposed by Marten-Wells [32]. This VSF has been confirmed for small angles and the choice of  $\alpha_0 = 0.03rad$

$$\beta(\alpha) = \frac{\alpha_0}{2\pi(\alpha_0^2 + \alpha^2)^{3/2}}. \quad (3.3)$$

This formula provides a good fit to available data for seawater (with no turbulence). The resultant VSF are presented in Figure 3.3.

### 3.3 Interaction of light with oceanic temperature inhomogeneities

Another mechanism of light scattering in the ocean is the scattering on turbulent inhomogeneities, which lead to fluctuations in the index of refraction. In general the effects of turbulence on the light beam appear (for two extreme beam diameters) in two forms: for wide light beams (wider than small temperature scales) the initially uniform light beam becomes ‘granular’, *i.e.* exhibits spatial non-uniformity due to focusing on turbulent inhomogeneities. In the case of thin light beams turbulence causes beam wandering or ‘jitter’. Due to technical problems it is experimentally difficult to measure these effects. Any minor imperfection in the optical system is likely to affect the measurements, making such observations unreliable [74]. Thus we have chosen to quantify the effect of turbulence on scattering using a numerical simulation of the turbulent flow field and of light propagation.

### 3.4 Light scattering on turbulent flow

Maxwell’s equation governs the propagation of a light beam through a turbulent medium. The magnetic permeability of water is negligible while the dielectric constant (refractive index) is assumed to be space variant and the effect of depolarization

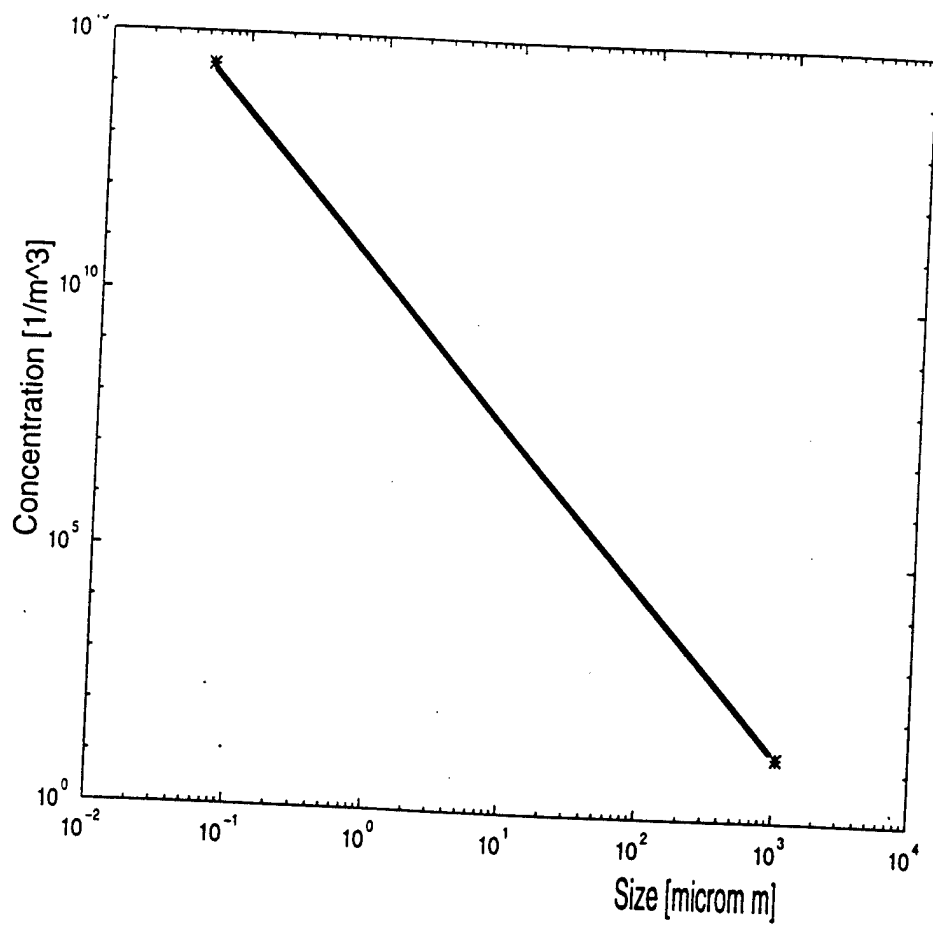


Figure 3.2: Size distribution of typical particulate concentrations following Brown and Gordon's measurements [1974].

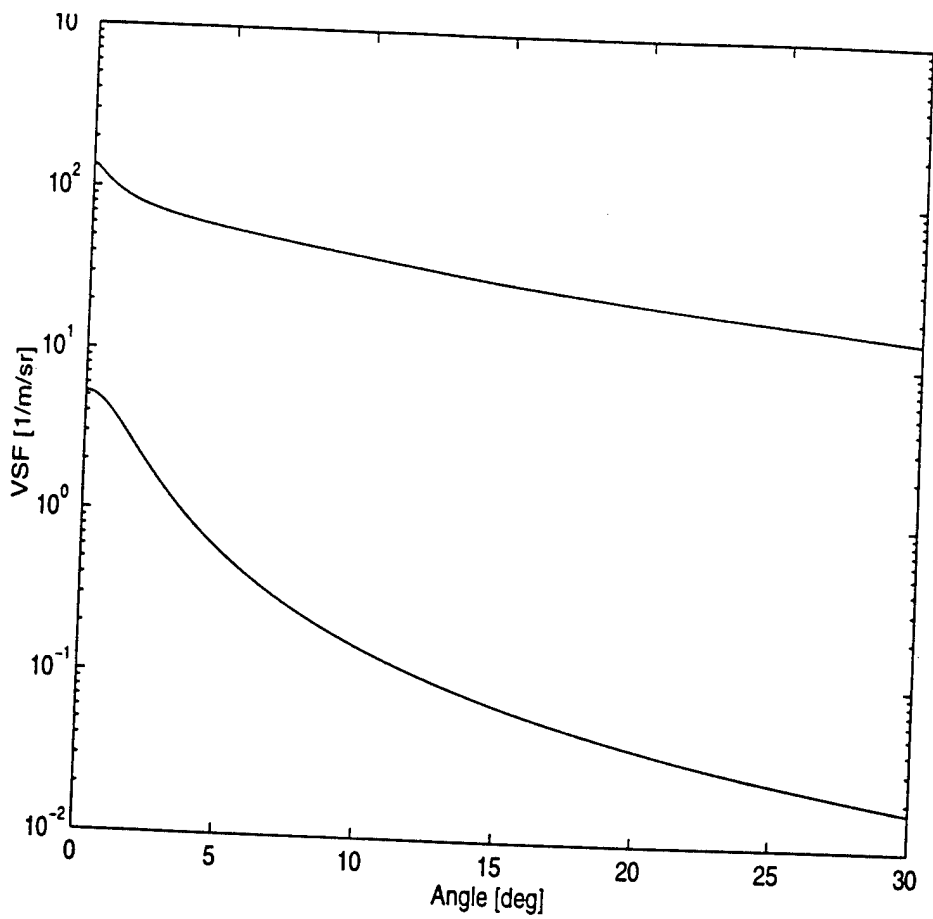


Figure 3.3: Particulate VSF for coastal and open ocean particulate concentrations.

is negligible. If backscatter is not important, then light propagation is described by the parabolized (diffusion-like) Helmholtz equation [69],

$$2ik \frac{\partial \psi}{\partial z} + \nabla_T^2 \psi + 2k^2 n' \psi = 0, \quad (3.4)$$

where  $\psi(r)$  is the phase of the propagating light, and  $z$  is taken along the direction of light propagation,  $\nabla_T^2$  is the transverse Laplacian operator, and  $k = 2\pi/\lambda$  where  $\lambda$  is the wavelength and  $n'$  is the deviation of the local refractive index from its mean value. Several approximation techniques have been developed for this equation [35], however I have solved this equation exactly using a developed numerical algorithm.

Further simplifications to equation (3.4) can be applied if we are interested in propagation over short distances. If the distance of propagation  $L$  (in our calculations 0.25 m) obeys  $(L\lambda)^{1/2} \ll \eta$ , where  $\eta$  is the scale of smallest temperature structure of the flow (typically of  $O(mm)$ ), and diffraction effects are neglected [69], the transverse Laplacian operator can be omitted and the above equation can be solved analytically:

$$\psi(x, y) = A_0(x, y) \exp \left( -ik \int_0^L n'(x, y, z) dz \right) \quad (3.5)$$

where  $A_0$  is initial value of  $\psi(x, y, z)$  at  $z = 0$ . This solution constitutes the first order geometrical optics approximation [69]. Since the second derivatives have been neglected in this approximation only changes in phase can be calculated. This is a sufficient simplification for the present study, since I am mostly interested in the light scattering angle for propagation distances over a few tenths of cm. To verify if the geometrical optics approximation (Eq. 3.5) used in this work is appropriate over the investigated parameter range of distances and turbulent flows we have validated it experimentally by comparing the exact numerical solutions of full Eq. (3.4) [6].

The light phase at the exit of the computational volume can be obtained with above equations and with knowledge of the spatial distribution of the refractive index inside the investigated volume. Since there is a simple relation between temperature and refractive index the spatial distribution of the temperature field is required.

### 3.5 Numerical simulation of the turbulent flow

Most geophysical flows usually have a large range of scales dependent on the Reynolds number of the flow. We thus must first determine which spatial scales of the flow are relevant for light scattering. For example an oceanic eddy presents temperature variability on scales ranging from  $O(10 \text{ m})$  down to  $1 \text{ mm}$ . The most intuitive approach to determine the optically-relevant range of scales can be obtained from geometrical optics. It can be shown that the change of the mean scattering angle variance  $\langle \alpha^2 \rangle$ , (the angle is taken between actual propagation direction and initial ray direction) per unit distance  $dr$  depends only on the details of the small scale temperature distribution in the absence of the large scale temperature gradients in the flow *i.e.*:

$$\frac{d\langle \alpha^2 \rangle}{dr} \propto \int_0^\infty E_T k dk \quad (3.6)$$

where  $dr$  is a small increment along the light beam,  $x$  is perpendicular to the light propagation coordinate, and  $E_T(k)$  is the 3-dimensional spectrum (in Fourier space  $-k$ ) of the temperature field  $T(r)$  (see the previous chapter). The largest contribution to the integral on the right hand side, for propagation distances of  $O(m)$  and the observed oceanic range of  $\epsilon$  values, comes from the smallest scales present in the turbulent field [5]. Therefore any numerical simulation of changes in the refractive index, here due to the temperature fluctuations, must reproduce these scales correctly to account for the most important scattering events.

We chose a model of homogeneous and isotropic turbulent flow to describe the inhomogeneities of the temperature field. This is the simplest turbulence model for which there exist theoretical solutions. However, it does not contain any large scale stable temperature gradients which may be present in actual ocean flows such as boundary layer flows.

### 3.6 Relevant turbulence parameters determining the light scattering at small angles on RII

As demonstrated earlier from a light propagation standpoint, the largest contribution to scattering comes from the smallest scales of the temperature  $E_T$  distribution (Eq.

3.6). In the previous chapter I have demonstrated that all flows containing the temperature as a passive scalar will result in a universal self-similar distribution of the temperature variance field at small scales; the universal distribution is given by the Kraichnan model, Eq. (2.30).

This spectral relationship is uniquely determined by two parameters,  $\epsilon$  and  $\chi$  which can be measured in the ocean [17]. The rate of dissipation of turbulent kinetic energy,  $\epsilon$ , determines the spatial size  $\eta$ , where  $\eta \simeq (\nu^3/\epsilon)^{1/4}$ , of the smallest temperature structure. The physical meaning of  $\chi$  ( $\chi = \int_0^\infty E_T k^2 dk$ ) is the rate at which the temperature fluctuations present in the flow dissipate [31]. From an optical perspective,  $\chi$  has the following interpretation: larger values correspond to stronger temperature gradients across the smallest temperature structure of the flow. This situation is pictorially represented in Figure 3.4. To summarize, the optical properties of a turbulent homogeneous and isotropic flow are characterized by two parameters:  $\chi$  which expresses the strength of the temperature gradient and  $\epsilon$  which is inversely proportional to the size of the smallest flow structure. Typically  $\chi$  ranges from  $10^{-2} \text{ } ^\circ C^2/s$  a few meters below the surface [19] to  $10^{-10} \text{ } ^\circ C^2/s$  in the mid water column [16]. For  $\epsilon$  the range is from  $10^{-4} m^2/s^3$  in a fairly energetic upper layer to  $10^{-11} m^2/s^3$  in mid water column [1].

The range and the vertical distribution of  $\chi$  and  $\epsilon$  values typical for the mid-part of the water column is shown in Figure 3.5 (J. Moum, pers. comm.). The scattered plot of observed  $\chi$  vs.  $\epsilon$  is shown in Figure 3.6. Note that the observed values of  $\chi$  vs.  $\epsilon$  are fairly uncorrelated.

### 3.7 Numerical experiment of light scattering on turbulent flow

As established in the previous chapter the temperature variance spectra at small scales are independent of the their source and depend on the parameters of the turbulent flow. Our procedure to propagate light through the turbulent flow is as follows. First I scale the strength of temperature fluctuations  $T(x, y, z)$  using Eq. 2.30 given the values of  $\chi$  and  $\epsilon$  and then convert it into a spatial distribution of the refractive index  $n'(x, y, z)$ . Then I illuminate the computational volume with

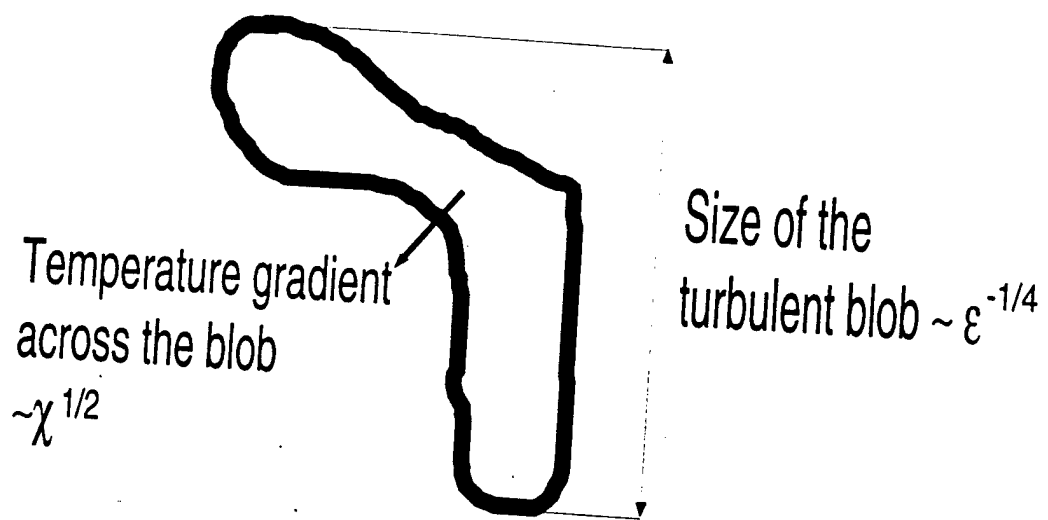


Figure 3.4: Optical interpretation of the turbulent parameters  $\chi$  and  $\varepsilon$ .

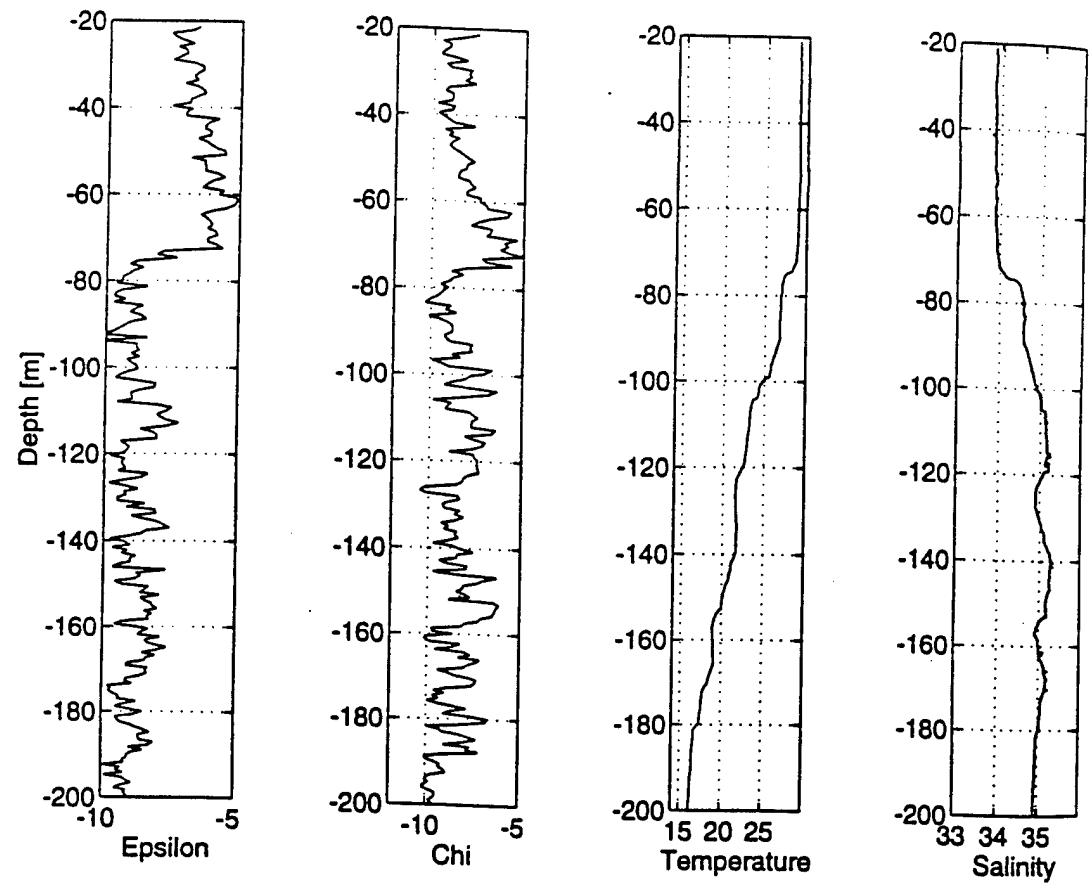


Figure 3.5: Profiles of  $\epsilon$ ,  $\chi$ , temperature and salinity from the Oregon coast (courtesy of J. Moum).

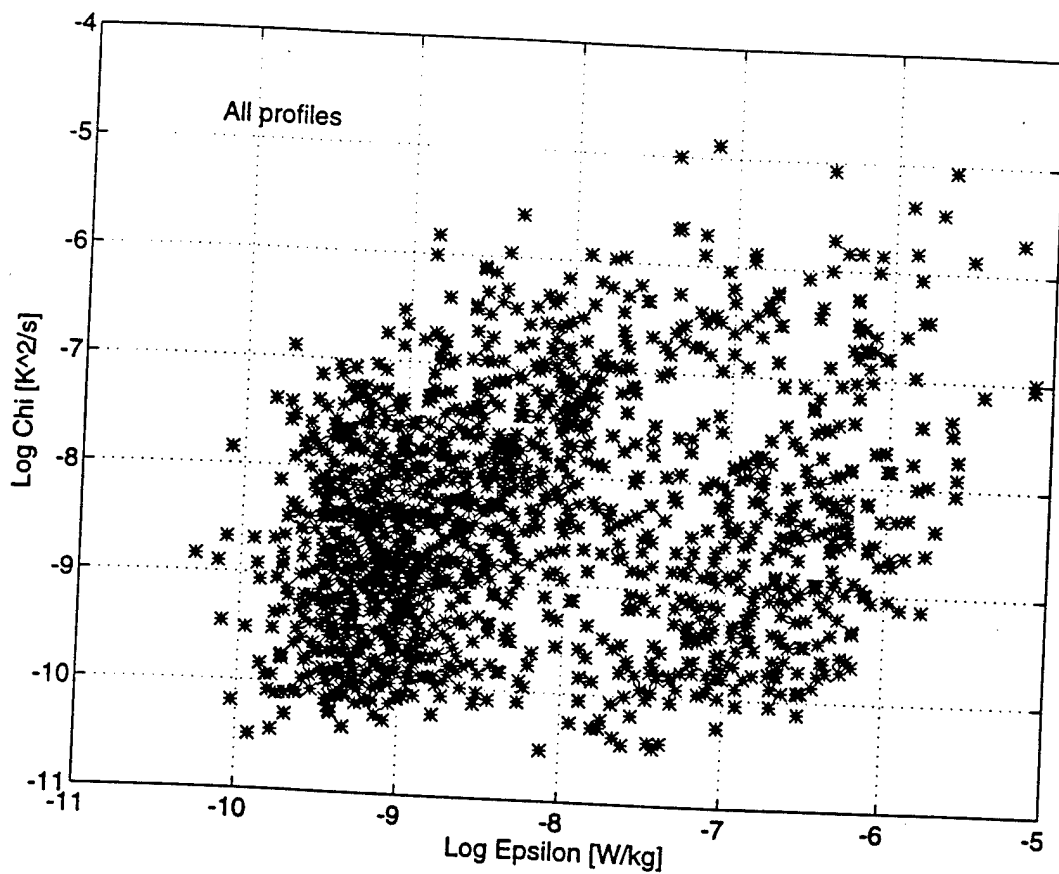


Figure 3.6: Scatter-plot of the observed  $\epsilon$  vs.  $\chi$  in the observational data set.

a plane parallel wave by assigning a constant value to the function  $\psi(x, y, z = 0)$ . Since I illuminate our computational volume ( $240^3$  size) with a plane parallel wave, the phase and amplitude of the light is the same throughout the entrance plane. We then use Eq. (3.5) (or Eq. (3.4) for verification) to estimate the resultant phase distortion  $\psi(x, y)$  of light on the exit side of the computational volume.

The imaginary value taken by  $\psi$  at each  $x, y$  position describes how the initially plane-parallel wavefront has been distorted by passage through the temperature inhomogeneities of the computational volume. The real part (different from  $A_0$  only if I solve Eq. (3.4)) describes the amplitude fluctuations. I show an example of the calculated distribution of light intensity at the exit estimated using Eq. (3.4) in [6]. It can be seen there that the initially homogeneous light beam becomes spatially inhomogeneous due to the effect of turbulence-induced scattering alone.

The imaginary part of  $\psi(x, y)$  carries information about scattering angle of the light beam. The vector normal to the isosurface  $z = \psi(x, y)$  is  $\bar{N}$ :

$$\bar{N} = \left[ \frac{\partial \psi}{\partial x}, \frac{\partial \psi}{\partial y}, -1 \right] \quad (3.7)$$

and is parallel to the outgoing ray direction. Since the exit surface has  $240^2$  different elements (of different  $\bar{N}$ ), our resolution is limited to this number when determining the VSF. The final calculation of the VSF is done in a straightforward manner from Eq. 3.1. The calculated VSF for extremal (large  $\chi$ ) conditions of  $\chi$  and  $\epsilon$  in the coastal ocean is given in Figure 3.7. From Figure 3.7 it can be seen that the VSF for any given  $\chi$  and  $\epsilon$  can be approximated by a Gaussian function, determined by flow-dependent parameters:

$$VSF(\epsilon, \chi, \alpha) = V_0(\epsilon, \chi) \cdot \exp(-(\alpha/\alpha_0(\epsilon, \chi))^2), \quad (3.8)$$

where  $V_0$  describes the maximum value of VSF at  $\alpha = 0$  and  $\alpha_0$  is the half-width.

The scattering angle variance ( $\langle \alpha^2 \rangle^{1/2}$ , calculated with respect to its initial direction, is also estimated as a diagnostic quantity. The value of the scattering angle variance depends on the propagation distance so I use a constant optical path 0.25m.

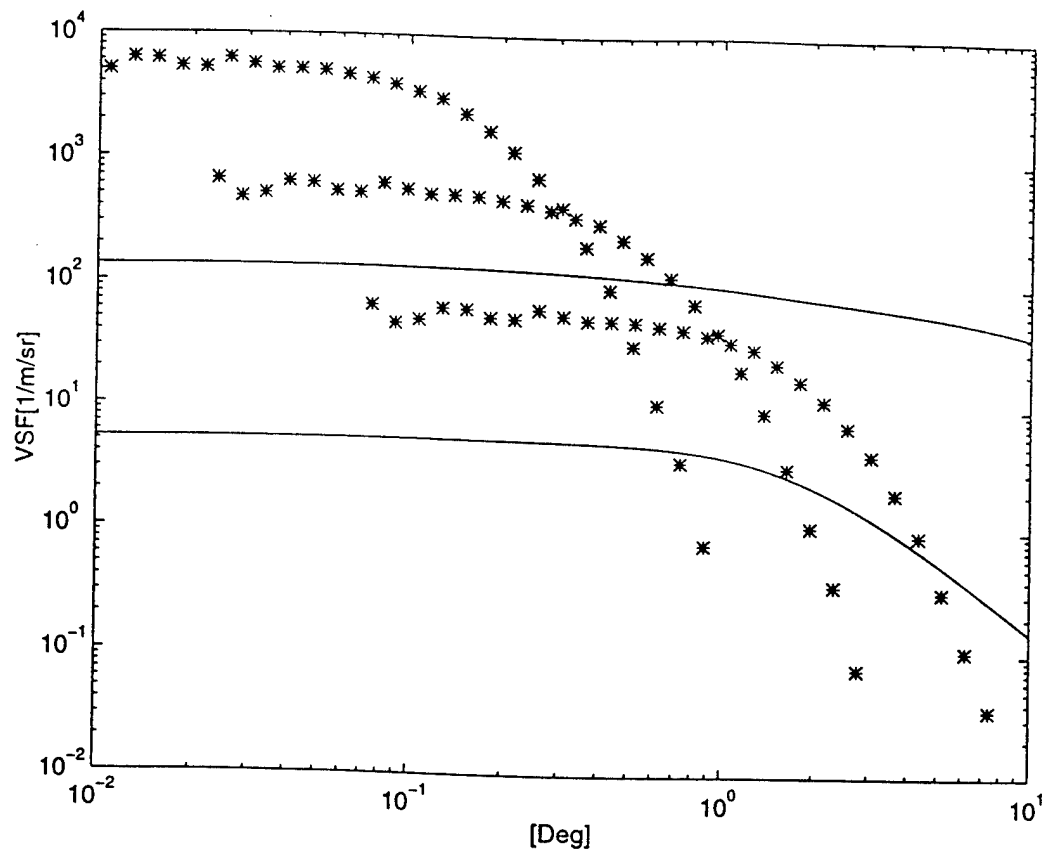


Figure 3.7: Simulated extreme VSF for a range of turbulent flows in the coastal regime or sea surface: a range of  $\chi$  and constant  $\epsilon = 10^{-10} \text{ m}^2/\text{s}^3$ . The solid lines denotes particulate VSF.

To obtain scattering angle variance  $(\langle \alpha^2 \rangle)^{1/2}$  for longer propagation distances  $L$ , the following formula can be used [45]:

$$(\langle \alpha^2 \rangle)^{1/2}(L, \chi, \epsilon) = C_{0.25}(\chi, \epsilon) \cdot (L/L_0)^{1/2}, \quad (3.9)$$

where  $L_0$  in case of my simulations is 0.25 m. The values of  $V_0$ ,  $\alpha_0$  and  $C_{0.25}(\chi, \epsilon)$  - scattering angle variance has been calculated for different flow conditions and is shown in Table 3.1.

$\log_{10} \epsilon$	$\log_{10} \chi$	$V_0$	$\alpha_0$ [deg]	$C_{0.25}(\chi, \epsilon)$ [rad]
-10	-2	$2 * 10^3$	$1.1 * 10^{-1}$	$10^{-3}$
-10	-4	$2 * 10^5$	$1.1 * 10^{-2}$	$10^{-4}$
-10	-6	$2 * 10^7$	$1.1 * 10^{-3}$	$10^{-5}$
-8	-2	$2 * 10^5$	$5 * 10^{-2}$	$5 * 10^{-4}$
-8	-4	$2 * 10^7$	$5 * 10^{-3}$	$5 * 10^{-5}$
-8	-6	$2 * 10^9$	$5 * 10^{-4}$	$5 * 10^{-6}$
-6	-2	$2 * 10^6$	$1.1 * 10^{-2}$	$2.5 * 10^{-4}$
-6	-4	$2 * 10^8$	$1.1 * 10^{-3}$	$2.5 * 10^{-5}$
-6	-6	$2 * 10^{10}$	$1.1 * 10^{-4}$	$2.5 * 10^{-6}$

Table 3.1: VSF( $V_0, \alpha_0$ ) and the scattering angle variance ( $\langle \alpha^2 \rangle$ ) $^{1/2}$  for 0.25 m path-length.

### 3.8 Comparison of VSF for particulates and turbulence in the coastal zone

The VSF corresponding to particulates obtained earlier can be compared with the VSF corresponding to energetic turbulence of the coastal ocean. From Table 3.1 we can see that the turbulent flow scatters light most when  $\chi$  is large and  $\epsilon$  is low. If we assume that  $\chi$  is driven by the mean gradient and a turbulent time scale ( $u'/L$ ), where  $u'$  is the typical rms current velocity and  $L$  is a characteristic length scale (for example the depth of the water column or a mixed layer depth is of  $O(10\text{ m})$  in the coastal region), we obtain the relationship  $\chi \simeq \delta T^2/(u'/L)$ , where  $\delta T$  is a mean temperature gradient. From this argument, I obtain values for  $\chi$  of  $10^{-2}\text{ }^{\circ}\text{C}^2/\text{s}$  and lower. This is consistent with measurements made by Farmer and Gemmrich [19] in the surface layer (upper few meters) of open ocean. The coastal value of  $\epsilon$  can be given analogously by  $\epsilon \simeq u'^3/L$  [70] and can be as high as  $10^{-4}\text{m}^2/\text{s}^3$  and as low as in the presented data set shown in Fig. 3.5.

Using the higher limit values of  $\chi$ , I have estimated the VSF for a range of  $\chi$  and for constant  $\epsilon = 10^{-10}\text{m}^2/\text{s}^3$ , value which is likely to be encountered in the coastal region or in the open ocean (Figure 3.7). For comparison the VSF corresponding to the particulates of the coastal ocean and open ocean are also plotted. It is clearly shown that in our simulations of the coastal zone, turbulence scattering can dominate to angles as large as  $5^\circ$ . The implications for underwater visibility applications are considerable as the scattering angle variance ( $\langle \alpha^2 \rangle$ ) $^{1/2}$ , is up to  $O(0.001\text{ rad})$  (Table 3.1) implying that over a range of  $10\text{m}$  the smallest detail which can be resolved has a size of  $O(0.1\text{m})$ . Since the surface layer of the open ocean shares turbulence characteristics with those of the coastal zone, the VSF also describes the surface open ocean. Turbulence dominates scattering for angles of  $10^\circ$ . The visibility through the turbulent surface of thickness  $10\text{m}$  is also going to be limited (in absence of other effects) to detail the extent of  $O(0.1\text{m})$ .

### 3.9 Experimental validation

To qualitatively validate the calculated VSF, I carried out a simple laboratory experiment at the laboratory facility of WetLabs (Philomath, Oregon). The source of turbulence was a convective cell and the optical measurements were made using the bench-top Variable Aperture Beam Attenuation Meter (VABAM) developed by WetLabs.

Turbulence for the experiment was generated by a simple convective cell created by a heated element on the bottom and a cooling element on the top. The applied temperature gradient corresponded to a Rayleigh number of  $O(10^8)$ , thus ensuring that the flow was fully turbulent. The corresponding  $\chi$  ranged from  $10^{-2}$  down to  $10^{-4} \text{ } ^\circ\text{C}^2/\text{s}$  and  $\epsilon$  values were between  $10^{-6}$  to  $10^{-8} \text{ m}^2/\text{s}^3$ . These wide ranges result from the temperature measurement system and the poor temporal and spatial uniformity of the heating/cooling setup. The large range also implies that the turbulent flow was inhomogeneous and anisotropic and therefore not well controlled.

The light path in VABAM starts at the flash lamp source, goes through a monochromator ( $\simeq 420\text{nm}$ ) and then a  $0.7\text{ mm}$  pinhole aperture to be collimated by a  $200\text{ mm}$  lens. It then passes through a beam splitter into the  $25\text{ cm}$  sample volume. The beam is focussed by another  $200\text{ mm}$  lens (with iris aperture is driven by a stepper motor) and impinges upon a diffuser plate followed by a large area detector. The minimum aperture diameter of the iris of the receiver lens defines the acceptance angle of the receiver. It is  $1.2\text{ mm}$ , which results in a  $0.12^\circ$  acceptance angle in water. The step resolution of the stepper motor is approximately  $1\text{ mm}$ ; thus the resolution of the acceptance angle ranges from approximately  $0.1$  to  $3^\circ$ . The sampling frequency is  $1\text{ Hz}$ .

The presence of turbulence in the sample volume caused very intermittent readings at all apertures; the largest variability was observed for the smallest aperture. The intermittency of the detected light is shown in Figure 3.8. Because of this extreme intermittency, a statistically stable value of the VSF could only be obtained by averaging. We calculated the VSF using data from a run of over an hour time period. The average becomes stable after averaging hundreds of readings over a couple of minutes and is shown in Figure 3.9.

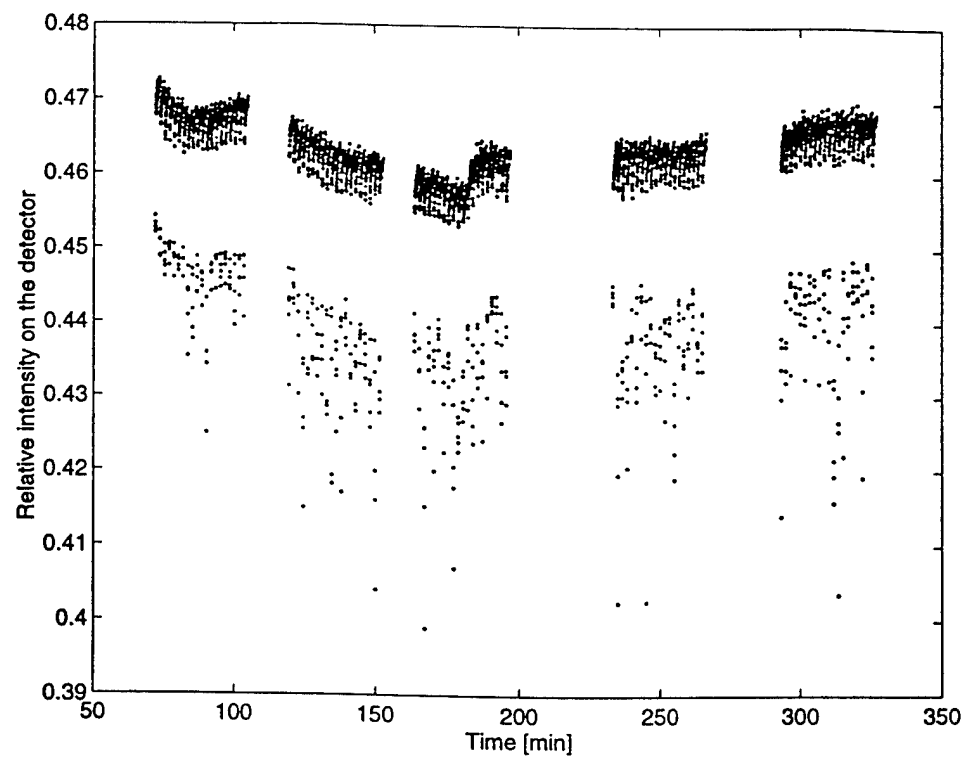


Figure 3.8: Time series of VABAM detector readings for two apertures. The smaller aperture corresponds to the larger variance

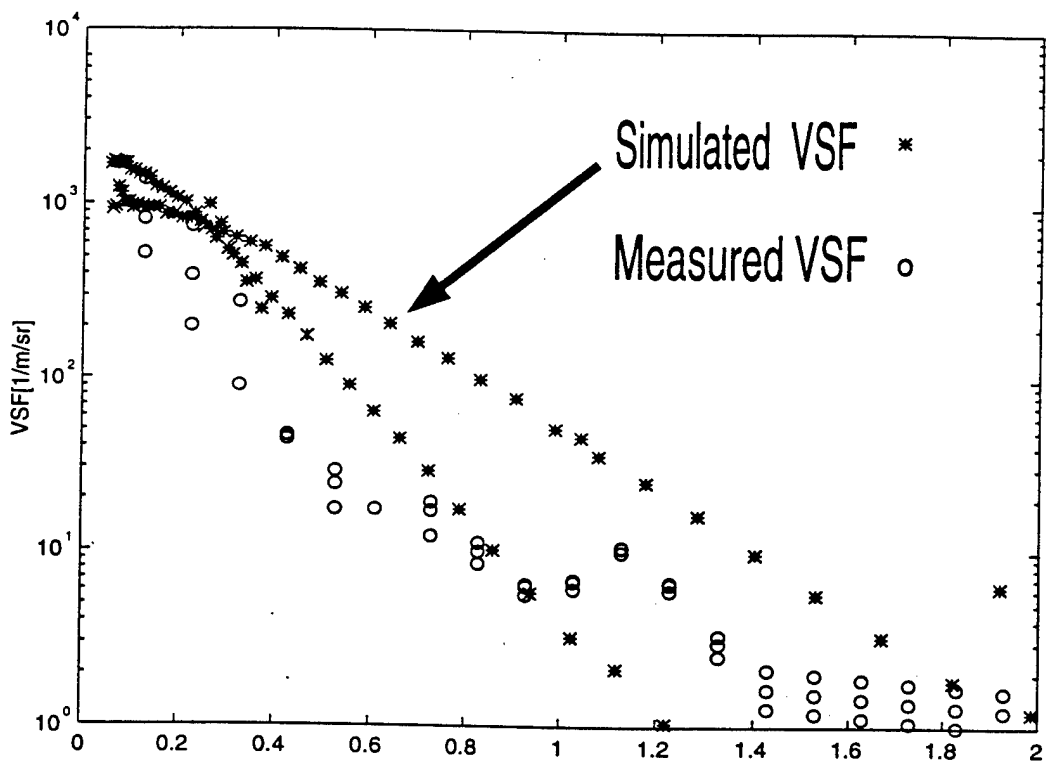


Figure 3.9: Experimentally measured VSF (circles) in the presence of turbulence temperature inhomogeneities and the simulated VSF (stars) for the corresponding values of  $\epsilon$  and  $\chi$ .

To evaluate the effect of particles,  $15 \mu\text{m}$  beads were added to the fairly weak turbulent flow. In another experiment this concentration resulted in a visible increase of the VSF (consistent with Mie theory) in runs with no turbulence [50]. However, in the weak turbulent regime the VSF remained larger than Mie predictions and there was no change in VSF after adding the beads.

It should be kept in mind that in theory the VSF is obtained as a limit when the pathlength goes to zero. Usually measurements are done over a small volume  $V$  and the outcome of the calculated VSF should not depend on the volume size. In the case of the scattering on turbulence this is not true. Since turbulence has an associated length-scale  $\eta$ , every near-forward VSF measurement will depend not only on turbulent quantities  $\eta$  and  $\chi$  but also on the size of the volume itself. This situation makes comparison of near-forward VSF measurements from different volumes difficult, especially when made from different instruments.

Even though our experimentally measured VSF agrees qualitatively with the simulation it is difficult to compare the two for several reasons. Turbulence simulations correspond to homogeneous isotropic turbulence, the values of  $\chi$  and  $\epsilon$  are precisely determined, and I have only one realization of the temperature field. By contrast, the turbulence of the experiment is not homogeneous; I cannot provide precise values of  $\chi$  or  $\epsilon$ , and many realizations of the temperature field are averaged throughout the course of the experiment into one VSF value. We know from the simulations that the slope of VSF is very sensitive to the value of the turbulent parameters  $\chi$  and  $\epsilon$  which precludes exact predictions for our experiment.

The most important outcome of the experiment is the confirmation that turbulence indeed dominates scattering at small angles of  $O(1^\circ)$  and that scattering can be well modeled using our numerical DNS database. A striking result is that the value of the VSF at small angles is highly intermittent. Any measurement technique which relies on angles of  $O(1^\circ)$  or less must develop an appropriate averaging scheme. This intermittency can only be attributed to turbulence. Another major conclusion was that turbulent scattering was found to be strong enough to account for the observed values of the near-forward VSF. The example of *in situ* measurement affected by near-forward light scattering on turbulence is the measurement of beamC. To minimize influence of turbulence the several instantaneous beamC readings should be averaged into one value.

In spite of the large uncertainties of the experimental turbulence quantities, these values are highly consistent with the numerically simulated VSF. This experimental confirmation of the predicted VSF can help us to understand light propagation for example in the coastal zone.

### 3.10 Conclusions

- Turbulent scattering dominates particulate scattering up to  $5^\circ$  in the coastal zone and to  $10^\circ$  in the upper layer of the open ocean.
- The turbulence can limit underwater visibility to details of size  $O(0.1m)$  for a range of 10 meters.
- Since turbulent flows are highly intermittent this results in high variance in the value of the VSF at small angles.
- Measurement of the VSF in the near-forward direction depends on the volume and flow characteristics of the sampling volume.
- Our numerical simulations were supported by the preliminary experiment. A future experiment should include a more comprehensive control of turbulent parameters.

### 3.11 Summary

We have investigated numerically and experimentally the scattering of a light beam at small angles. I compare the effects of scattering by typical coastal and oceanic particulate distributions with turbulence-induced scattering. I find that turbulence dominates scattering up to  $5\text{--}10^\circ$  for the coastal region and for the upper layer of the open ocean. Our preliminary experiment confirms predictions that the frequently observed high *in situ* values of the volume scattering function at small angles are related to scattering on turbulent inhomogeneities in seawater. Furthermore, the initially homogeneous light becomes spatially inhomogeneous and highly intermittent after propagating through the turbulent region. This intermittence will affect

single realization measurements by increasing the variance. In addition I confirmed that the mean scattering angle depends strongly on  $\chi$ .

## Reference List

- [1] A. Anis and J. N. Moum. Surface wave-turbulence interactions: scaling  $\epsilon(z)$  near the sea surface. *J. Phys. Oceanogr.*, 25:2025–2045, 1995.
- [2] T. M. Antonsen, Z. F. Fan, and E. Ott.  $k$  spectrum of passive scalars in Lagrangian chaotic fluid flows. *Phys. Rev. Lett.*, 75:1751–1754, 1995.
- [3] G. K. Batchelor. Small scale variation of convected quantities like temperature in a turbulent fluid. *J. Fluid Mech.*, 5:113–133, 1959.
- [4] G. K. Batchelor, I. D. Howells, and A. A. Townsend. Small scale variation of convected quantities like temperature in a turbulent fluid. The case of large conductivity. *J. Fluid Mech.*, 5:134–139, 1959.
- [5] D. Bogucki, A. Domaradzki, and P. K. Yeung. Direct numerical simulations of passive scalars with  $\text{Pr} > 1$  advected by turbulent flow. *Journal of Fluid Mechanics (submitted)*.
- [6] D. J. Bogucki, A. Domaradzki, R. Zaneveld, and T. Dickey. Light scattering induced by turbulent flow. *SPIE Proceedings, Ocean Optics XII*, 2258:247–255, 1994.
- [7] C. F. Bohren and D. R. Huffman. *Absorption and Scattering of Light by Small Particles*. John Wiley and Sons, New York, 1983.
- [8] M. Born and E. Wolf. *Principles of Optics*. Pergamon Press, Oxford, 1964.
- [9] O. B. Brown and H. R. Gordon. Size refractive index distribution of clear coastal water particulates from light scattering. *Applied Optics*, 13:2874–2881, 1974.
- [10] D. R. Caldwell, T. M. Dillon, J. M. Brubaker, P. A. Newburger, and C. A. Paulson. The scaling of vertical temperature gradient spectra. *J. Geophys. Res.*, 85:1917–1924, 1980.
- [11] J. Chasnov, V. M. Canuto, and R. S. Rogallo. Turbulence spectrum of a passive temperature field: results of a numerical simulation. *Phys. Fluids*, 31:2065–2067, 1988.

- [12] S. Chen, G. Doolen, J.R. Herring, R.H. Kraichnan, S.A. Orszag, and Z.S. She. Far dissipation range of turbulence. *Phys. Rev. Lett.*, 70:3051–3054, 1993.
- [13] J. P. Clay. Turbulent mixing of temperature in water, air and mercury. *Ph.D. thesis, University of California at San Diego*, 1973.
- [14] S. Corrsin. On the spectrum of isotropic temperature fluctuations in isotropic turbulence. *J. Appl. Phys.*, 22:469, 1951.
- [15] S. Corrsin. Further generalization of Onsager's cascade model for turbulent spectra. *Phys. Fluids*, 7:1156–1159, 1964.
- [16] T. M. Dillon. The energetics of overturning structures: Implications for the theory of fossil turbulence. *J. Phys. Oceanogr.*, 14:541–549, 1984.
- [17] T. M. Dillon and D. R. Caldwell. The Batchelor spectrum and dissipation in the upper ocean. *J. Geophys. Res.*, 85:1910–1916, 1980.
- [18] J. A. Domaradzki. Nonlocal triad interactions and the dissipation range of isotropic turbulence. *Phys. Fluids A*, 4:2037–2045, 1992.
- [19] D. M. Farmer and J. R. Gemmrich. Measurements of temperature fluctuations in breaking surface waves. *J. Phys. Oceanogr.*, 26:816–825, 1996.
- [20] A. Gargett. Evolution of scalar spectra with the decay of turbulence in a stratified fluid. *J. Fluid Mech.*, 159:379–401, 1985.
- [21] C. H. Gibson. Fine structure of scalar fields mixed by turbulence. I . Zero-gradient points and minimal gradient surfaces. *Phys. Fluids*, 11:2305–2315, 1968.
- [22] C. H. Gibson. Fine structure of scalar fields mixed by turbulence. II . Spectral theory. *Phys. Fluids*, 11:2316–2327, 1968.
- [23] C. H. Gibson. Kolmogorov similarity hypotheses for scalar fields: sampling intermittent turbulent mixing in the ocean and galaxy. *Proc. R. Soc. Lond. A*, 434:149–164, 1991.
- [24] C. H. Gibson and W. H. Schwarz. The universal equilibrium spectra of turbulent velocity and scalar fields. *J. Fluid Mech.*, 16:365–384, 1963.
- [25] J. P. Gollub, B. S. Williams, and D. Martean. Scalar mixing in disorder 2-D vortex flows. *Bull. Am. Phys. Soc.*, 40:1924, 1995.
- [26] H. R. Gordon. Sensitivity of radiative transfer to small-angle scattering in the ocean: quantitative assessment. *Applied Optics*, 32:7505–7511, 1993.

- [27] H. L. Grant, B. A. Hughes, R. B. Williams, and A. Moilliet. The spectrum of temperature fluctuations in turbulent flow. *J. Fluid Mech.*, 34:423–442, 1968.
- [28] M. C. Gregg. Diapycnal mixing in the thermocline: a review. *J. Geophys. Res.*, 92:9686–9698, 1987.
- [29] J. R. Herring and R. M. Kerr. Comparison of direct numerical simulations with predictions of two-point closures for isotropic turbulence convecting a passive scalar. *J. Fluid Mech.*, 118:205–219, 1982.
- [30] R. J. Hill. Models of the scalar spectrum for turbulent advection. *J. Fluid Mech.*, 88:541–562, 1978.
- [31] J. O. Hinze. *Turbulence: An Introduction to Its mechanism and Theory*. McGraw-Hill, New York, 1959.
- [32] H. Hodara. *Experimental Results of Small - Angle Scattering*. AGARD Lect. ser. 61, NATO, 1973.
- [33] M. Holzer and E. D. Siggia. Turbulent mixing of a passive scalar. *Phys. Fluids*, 6:1820–1837, 1994.
- [34] R. C. Honey and G. P. Sorensen. pages 39–39.7. AGARD Conf. Proc. No. 77, 1970.
- [35] R. E. Hufnagel and N. R. Stanley. Modulation transfer function associated with image transmission through turbulent media. *Journal of the Optical Society of America*, 54(1):52–61, 1963.
- [36] R. M. Kerr. High-order derivative correlations and the alignment of small-scale structures in isotropic numerical turbulence. *J. Fluid Mech.*, 153:31–58, 1985.
- [37] R. M. Kerr. Velocity, scalar and transfer spectra in numerical turbulence. *J. Fluid Mech.*, 211:309–332, 1990.
- [38] S. Kida and Y. Murakami. Kolmogorov similarity in freely decaying turbulence. *Phys. Fluids*, 30:2030–2039, 1987.
- [39] R.H. Kraichnan. The structure of isotropic turbulence at very high Reynolds numbers. *J. Fluid Mech.*, 5:497, 1959.
- [40] R.H. Kraichnan. Small-scale structure of a scalar field convected by turbulence. *Phys. Fluids*, 11:945, 1968.
- [41] Y. A. Kravtsov. New effects in wave propagation and scattering in random media (a mini review). *Applied Optics*, 32:2681–2691, 1993.

- [42] E. Kunze, A. J. Williams, and R. W. Schmitt. Optical microstructure in the thermohaline staircase east of Barbados. *Deep-Sea Research*, 34:1697–1704.
- [43] M. Lesieur. *Turbulence in Fluids*. Martinus Nijhoff Publishers, 1990.
- [44] D.O. Martinez, S. Chen, G.D. Doolen, R. Kraichnan, L.P. Wang, and Y. Zhou. Energy spectrum in the dissipation range of turbulence. *Phys. Rev. E*, submitted, 1996.
- [45] L. E. Mertens. *In water photography - theory and practice*. Wiley Interscience, 1970.
- [46] O. Metais and M. Lesieur. Spectral large-eddy simulation of isotropic and stably stratified turbulence. *J. Fluid Mech.*, 239:157–194, 1992.
- [47] P. L. Miller and P. E. Dimotakis. Measurements of scalar power spectra in high Schmidt number turbulent jets. *J. Fluid Mech.*, 308:129–146, 1995.
- [48] R. C. Mjolsness. Diffusion of a passive scalar at large Prandtl number according to the abridged Lagrangian interaction theory. *Phys. Fluids*, 18:1393–1394, 1975.
- [49] A. S. Monin and A. M. Yaglom. *Statistical Fluid Mechanics: Mechanics of Turbulence*. The MIT press, 1981.
- [50] C. Moore. Variable Aperture Beam Attenuation Meter. Technical report, ONR annual Report, 1995.
- [51] A. Morel and A. Bricaud. Inherent properties of algal cells including picoplankton: theoretical and experimental results. In T. Platt and W.K.W. Li, editors, *Photosynthetic Picoplankton*, pages 521–559. Canadian Journal of Fisheries and Aquatic Sciences, 214, 1986.
- [52] G. R. Newman and J. R. Herring. A test field study of a passive scalar in isotropic turbulence. *J. Fluid Mech.*, 94:163–194, 1979.
- [53] N. S. Oakey. Determination of the rate of dissipation of turbulent energy from simultaneous temperature and velocity shear microstructure measurements. *J. Phys. Oceanogr.*, 12:256–271, 1982.
- [54] A. M. Obukhov. Structure of the temperature field in turbulent flows. *Isv. Geogr. Geophys. Ser.*, 13:58–69, 1949.
- [55] T. H. Petzold. Volume scattering functions for selected ocean waters. *Technical report, U. of California San Diego*, 1972.
- [56] R. W. Preisendorfer. *Hydrologic Optics, Vol. 1 (Introduction)*. NOAA, 1976.

- [57] A. Pumir. Small scale properties of scalar and velocity differences in three-dimensional turbulence. *Phys. Fluids*, 6:3974–3984, 1994.
- [58] J. Qian. Viscous range of turbulent scalar of large Prandtl number. *Fluid Dynamics Research*, 15:103–112, 1995.
- [59] J. B. Riley. Laser diffraction particle sizing: sampling and inversion. *Ph.D. thesis, MIT-Woods Hole Joint Program in Ocean Engineering*, 1987.
- [60] R. S. Rogallo. Numerical experiments in homogeneous turbulence. *NASA Technical Memorandum*, 81315, 1981.
- [61] G. R. Ruetsch and M. R. Maxey. Small - scale features of vorticity and passive scalar fields in homogenous isotropic turbulence. *Phys. Fluids A*, 3:1587–1597, 1991.
- [62] K. S. Shifrin. *Physical Optics of Ocean Water*. AIP Translation Series, New York, 1988.
- [63] Spinrad, R. W., J. R. Zaneveld, and H. Pak. Volume scattering function of suspended particulate matter at near-forward angles: a comparison of experimental and theoretical values. *Applied Optics*, 17:1125–1135, April 1978.
- [64] R. W. Spinrad, H. Glover, B. B. Ward, L. A. Codispoti, and G. Kullenberg. Suspended particle and bacterial maxima in Peruvian coastal waters during a cold water anomaly. *Deep-Sea Research*, 14:715–733, 1989.
- [65] K.R. Sreenivasan. On the fine-scale intermittency of turbulence. *J. Fluid Mech.*, 151:81, 1985.
- [66] D. Stramski and D. A. Kiefer. Light scattering by microorganisms in the open ocean. *Prog. Oceanogr.*, 28:343–383, 1991.
- [67] J. W. Strohbehn. Modern theories in the propagation of optical waves in a turbulent medium. In J. W. Strohbehn, editor, *Laser Beam Propagation in the Atmosphere*, pages 45–104. Springer-Verlag, 1978.
- [68] N. P. Sullivan, S. Mahalingam, and R.M. Kerr. Deterministic forcing of homogeneous, isotropic turbulence. *Phys. Fluids*, 6:1612–1614, 1994.
- [69] V. I. Tatarski. *Wave Propagation in Turbulent Media*. McGraw-Hill, New York, 1961.
- [70] H. Tennekes and J. L. Lumley. *A First Course in Turbulence*. MIT Press, Cambridge, Mass, 1972.

- [71] C. R. Truman. The influence of turbulent structure on optical phase distortion through turbulent shear flows. In *AIAA Technology Conference*. 1992.
- [72] B. J. Uscinski. *Wave Propagation and Scattering*. Clarendon Press, 1986.
- [73] L. A. Vasilev. *Schlieren Methods*. Israel program for scientific translations, 1971.
- [74] K. J. Voss and A. L. Chapin. Measurement of the point spread function in the ocean. *Applied Optics*, 29:3638–3642, 1990.
- [75] W. H. Wells. *Theory of Small-angle Scattering*, page Chap. 3.3. AGARD Lect. ser. 61, NATO, 1973.
- [76] P. K. Yeung and S. B. Pope. An algorithm for tracking fluid particles in numerical simulations of homogeneous turbulence. *J. of Comput. Phys.*, 79:531–586, 1988.
- [77] H. T. Yura. Small-angle scattering of light by ocean water. *Applied Optics*, 10(1):114–118, January 1971.
- [78] J.R.V. Zaneveld. *Variation of optical sea parameters with depth*. AGARD Lect. ser. 61, NATO, 1973.